Design, Fabrication and Testing of a Stacked Variable-Reluctance Motor

ARCHIVES
MASSACHUSETTS INSTITUTE OF TECHNOLOGY
OCT 29 2013
LIBRARIES

by

Kai Cao

B.S., Electrical Engineering, M.I.T. (2011)
B.S., Physics, M.I.T. (2011)

Submitted to the Department of Electrical Engineering and Computer Science
in partial fulfillment of the requirements for the degree of

Master of Engineering in Electrical Engineering and Computer Science

at the

MASSACHUSETTS INSTITUTE OF TECHNOLOGY

February 2013

© Massachusetts Institute of Technology 2013. All rights reserved.

Author ....
Department of Electrical Engineering and Computer Science
Nov 9, 2012

Certified by ....
Jeffrey H. Lang
Professor of Electrical Engineering and Computer Science
Thesis Supervisor

Accepted by ....
Dennis M. Freeman
Chairman, Masters of Engineering Thesis Committee

Design, Fabrication and Testing of a Stacked Variable-Reluctance Motor

by

Kai Cao

Submitted to the Department of Electrical Engineering and Computer Science
on Nov 9, 2012, in partial fulfillment of the
requirements for the degree of
Master of Engineering in Electrical Engineering and Computer Science

Abstract

A new type of variable-reluctance motor with axially stacked stator and rotor plates is explored in this thesis. This stacked variable-reluctance motor (SVRM) has mechanically parallel air gaps, carrying magnetic flux in series. Magnetic models are developed to predict the maximum and minimum flux linkage of the motor, as well as the average torque over an electrical cycle. A geometric optimization is carried out using a combination of the Monte Carlo method and the simulated annealing method on a prototype, designed as a hip motor for a cheetah like robot. A one-phase 56 pole-pair prototype is designed and constructed to confirm the theory. The prototype can maintain its two 100 μm axial air gaps over a 5 inch diameter. The prototype, given all its practical constraints, produces 2 Nm of torque at 30 A phase current. After material property adjustments, the model predictions match well with the experimental performance of the prototype. Another round of optimization is done using the modified material properties, the best torque-to-mass ratio found for a ferrite motor with no more than 100 pole pairs is 8.4 Nm/kg. It is concluded that ferrite's flux carrying capacity is insufficient for high toque-to-mass ratio motors, given the requirements of the hip motor. A steel SVRM can have torque-to-mass ratio as high as 35.7 Nm/kg, but is restricted to low speed operation due to the slow magnetic diffusion.

Thesis Supervisor: Jeffrey H. Lang
Title: Professor of Electrical Engineering and Computer Science

Acknowledgments

I would like to thank the Defense Advanced Research Projects Agency (DARPA) for its financial support. The thesis is funded via an award from DARPA managed by Boston Dynamics Inc.

I would like to thank my thesis and academic supervisor Professor Jeffrey Lang for his guidance throughout the entire project. His abundance of technical knowledge, his willingness to teach and his skills in communication are second to none. Many times during our weekly meetings, he would sit down and patiently explain a technical concept to me in such a concise and clear way that helped me learn the concept in minutes instead of days. I am also grateful for his encouragement and his resourcefulness when facing numerous challenges during the project.

I would like to thank the late Professor David Staelin who conceived this project. I valued his candor and enthusiasm greatly during the brief period he co-supervised me. May he rest in peace.

I would like to thank Professor Alexander Slocum and Professor David Trumper for their technical assistance in mechanical engineering. As a student majoring in EECS, my lack of mechanical engineering knowledge was apparent. I am very appreciative of their willingness to take time from their busy schedules to review my initially rudimentary design and point out the important design challenges. It would not have been possible to build the motor without their help. Professor Slocum's sense of humor was especially memorable.

I would like to thank Professor James Kirtley Jr. for teaching me what I know about electric machines in class and helping me with questions during this thesis project.

I would like to thank Brian Heberley and Anthony Wong for their assistance in using the CMM. Very few people would take that much time away from their own research to help someone else. Their generosity inspired me greatly.

I would like to thank Professor Ian Hunter and his PhD student Eli Paster for teaching me and letting me use their parylene coater. I deeply appreciate that they

opened up their lab to me, sometimes at almost unreasonable hours. I am grateful for their trust in me.

I would like to thank Ken Stone, Hayami Arakawa and Brian Chan for their help at the MIT Hobby Shop. I owe all my knowledge about the water jet to them.

I would like to thank Wayne Staats for his technical assistance in thermodynamics modeling. I met him while collaborating on another project. I will treasure the friendship we formed over the course of the two projects.

I would like to thank my close friends Sunshine Zhou and Sohan Mikkilineni for helping me editing my thesis. It is truly a privilege to have friends to whom you can talk about anything.

I would like to thank the MIT Solar Electric Vehicle Team for letting me use their resources. In addition, I would like thank all the friends I made there for bringing me joy and excitement while I was at MIT.

Finally, I would like to thank everyone else who gave me assistance during the project for their patience and understanding.

Contents

1 Introduction **17**

1.1 Thesis Motivation 18

1.2 Organization 19

1.3 Summary of Conclusions 20

2 Fundamentals **23**

2.1 Motor Types 23

2.2 Elementary Physics 28

  2.2.1 Magnetic Circuit 28

  2.2.2 Energy and Co-energy 30

2.3 Summary 33

3 Numerical Analysis and Design Optimization **35**

3.1 Motor Topology and Model Reduction 35

3.2 Materials 38

  3.2.1 Nonlinear Modeling of High-permeability Materials 38

  3.2.2 Skin Depth Consideration and Material Selection 40

3.3 Models 43

  3.3.1 Aligned Position (Maximum Inductance) Model 43

  3.3.2 Unaligned Position (Minimum Inductance) Model 48

  3.3.3 Total Model 50

3.4 Optimization Processes 53

  3.4.1 The Monte Carlo Method 55

3.4.2 The Simulated Annealing Method 56
3.4.3 Optimization Results 58
3.5 Summary 60

4 Mechanical Design and Fabrication **61**
4.1 Design Objectives 61
4.2 Mechanical Design 61
4.2.1 Bearing Design 61
4.2.2 Rotor Stiffness 67
4.3 Fabrication Processes 68
4.3.1 Stator, Rotor, Back Iron and Winding 68
4.3.2 Supporting Structure 72
4.3.3 Assembly 73
4.4 Summary 74

5 Experiments and Results **75**
5.1 Mechanical Measurements 75
5.1.1 Parallelism 75
5.1.2 Bearing Stiffness 79
5.1.3 Mechanical Conclusions 79
5.2 Magnetic Flux Linkage Measurements 80
5.2.1 Experimental Setup 80
5.2.2 Theory Comparison and Material Property Adjustment 83
5.3 Static Torque Measurements 87
5.3.1 Experimental Setup 87
5.3.2 Comparison with Theory 88
5.4 Optimization with Modified Permeability Curve 90
5.5 Summary 92

6 Conclusions **95**
6.1 Summary 95

6.2 Conclusions 96
6.3 Future Work 97

A Mechanical Drawings **99**

List of Figures

2-1 Axial-flux machine vs. radial-flux machine 24

2-2 (a) Misaligned, (b) aligned and (c) freewheeling rotor positions for a radial VRM. 25

2-3 (a) Misaligned, (b) aligned and (c) freewheeling rotor positions for an axial VRM. Back iron is not shown. 26

2-4 Rendering of one SVRM configuration.The blacks parts represent highly permeable core material and the orange parts represent copper wire. . 27

2-5 (a) C core with air gap, (b) equivalent magnetic circuit. 29

2-6 Schematic of a lossless magnetic field system. Adapted from [6]. . . . 30

2-7 Illustration of energy vs coenergy. 32

2-8 Comparison between energy and co-energy methods of calculating work done along a trajectory on the $\lambda - i$ plane. 33

3-1 3D drawing of the magnetic elements of SVRM, showing three stator plates and two rotor plates. Air gaps are not drawn to scale for illustration purposes. (a) isometric view (b) x-axis view. 36

3-2 Drawing of a section of the stator. The red box highlights one side of the unit cell. 37

3-3 3D drawings of the unit cell. (a) A wedge shaped unit cell. The curvature is exaggerated for illustration purposes. (b) Rectangular approximation of the unit cell. 37

3-4 Typical $B(H)$ curves for (a) steel [1] (b) ferrite 3C97 (Ferroxcube datasheet). Steel has much higher flux carrying capacity than ferrite. 39

3-5 Magnetic diffusion in stator poles. 41
3-6 Magnetic diffusion simulation results for Supermendur. 42
3-7 Magnetic diffusion simulation results for 3C97. 43
3-8 The unit cell in (a) the maximum inductance and (b) the minimum inductance position. 44
3-9 (a) Geometry of the aligned position (b) equivalent magnetic circuit. 45
3-10 FEA field solution of the aligned position. Note the absence of fringing field, as assumed for the analytical model. 46
3-11 Magnetic field energy calculated by COMSOL. 47
3-12 $\lambda - i$ curve for the aligned case. The FEA solution and the analytical solutions are very similar. At higher currents, the small difference between the FEA flux linkage and the analytical flux linkage is due to fringing fields. 48
3-13 FEA field solution of the unaligned position. 49
3-14 $\lambda - i$ curve for the unaligned case. 50
3-15 $\lambda - i$ trajectory during an electrical cycle. 52
3-16 Results from a typical Monte Carlo optimization for the motor design. Torque-to-mass ratio is in the units of [Nm/kg]. 56
3-17 A typical result from a SA optimization. Torque-to-mass ratio is in the units of $[Nm/kg]$. 58

4-1 Motor cross-section (a) CAD drawing (b) Schematic with parts labeled with colors. 62
4-2 Exploded view of the prototype. 63
4-3 (a) The perfect and (b) the most misaligned position for the rotor. . . 64
4-4 (a) zoomed-in view and the geometry of the bearing fitting and (b) the resulting geometry of the axle/rotor misalignment. The two large bold T's in the schematic represent the two axle/rotor positions shown in Figure 4-3. 65

4-5 Torque and axial force experienced by the a single rotor over an electrical cycle. The values are calculated directly using FEA for the prototype. The FEA average torque is very similar to what the theory predicts (See Chapter 5 for details of the comparison). 68
4-6 (a)Maximum z displacement (b) Maximum stress experience by the rotor. The deformation is exaggerated for illustration purposes. . . . 69
4-7 The flatness measurement of two sides of a 3C97 plate. 70
4-8 (a)Stator and (b)rotor after water jet cutting. 71
4-9 (a)Back iron plate (b)copper wingding with terminal masking. 72
4-10 Assembled (a) stator piece (b) stator & rotor piece. 74

5-1 Surfaces measured. (a)The housing plane was used as the reference plane for all other measurements. The results of (b), (c) and (d) are shown in Figure 5-3, Figure 5-2, Figure 5-4. 76
5-2 Errors in the parallelism of the stator surface. 77
5-3 Errors in the parallelism of the axle surface. 77
5-4 Measured error in the parallelism of the rotor (a)without and (b)with the axle nut. 78
5-5 Bearing stiffness measurements and the linear fitting. 80
5-6 Circuit schematic for flux linkage experiments. Component values are listed in Table 5.2. 81
5-7 RLC equivalent of the discharging circuit. 82
5-8 Initial comparison of maximum (aligned position) and minimum (unaligned position) flux linkage curves at $75\mu m$. 84
5-9 Comparison of maximum and minimum flux linkage curves at $75\mu m$ with modified permeability model. 85
5-10 Comparison of maximum and minimum flux linkage curves at $50\mu m$ and $100\mu m$ air gaps, with modified permeability curve and the rim effect. 86
5-11 Experimental setup for measuring static torque of the motor. 88

5-12 The flux pattern for a misaligned position. The force on the rotor poles can be directly calculated from the magnetic fields. 89
5-13 Torque produced at 30A over half of an electrical cycle with 100 μm air gaps. 90
5-14 Flux linkage versus current plot with modified permeability curve, but without rim effect adjustment. 91
5-15 Torque versus current at two different electrical angles. 92

List of Tables

3.1 Steps of the Monte Carlo optimization process 55

3.2 Steps of the simulated annealing optimization process 57

3.3 Optimal designs for different materials: (1) 3C97 with practical restrictions; (2) 3C97 without practical restrictions; (3) Supermendur. Note the weight in the torque-to-mass ratio does not involve the weight of motor casing and all other supporting structures. All motors are limited to at most 100 pole pairs. 60

4.1 Settings used in water jetting 3C97 ferrite 69

5.1 List of components used in the magnetic flux linkage measurement setup 83

5.2 Measured component values 83

5.3 List of components used in the static torque measurement setup . . . 87

5.4 Optimal designs with modified ferrite permeability for motor with 100 μm air gaps. 91

Chapter 1

Introduction

This thesis presents the design, fabrication and testing of a unique stacked variable-reluctance motor (SVRM), with axial parallel air gaps and serial magnetic flux. The choice of this architecture is aimed to increase the torque density and torque-to-mass ratio of the electric machine by utilizing the plurality of the air gaps. This thesis focuses on developing a design method that performs dimensional optimization using computer-aided design tools. A hybrid model that combines both lumped element method (LPM) and finite element analysis (FEA) is used to predict the flux linkage, and thus the torque produced in the SVRM. This model offers a good compromise between model accuracy and speed.

A case study of a robotic hip motor is used to validate the motor architecture and the theoretical model. The case study demands a motor that can achieve high torque density with minimum actuator impedance for applications with significant physical interactions with the environments. In addition, a high torque-to-inertia ratio is also important. A Monte Carlo optimization for torque-to-mass ratio is performed on a wide design space, and then a simulated annealing (SA) optimization is used to further narrow down the optimal design. A single phase prototype is built to verify the models. This thesis shows that the model prediction matches well with the prototype in the flux linkage and torque produced, after material property corrections.

1.1 Thesis Motivation

Electric motors, or motors which convert electrical power to mechanical power, have been one of the most essential and widely used technologies since the 1800s. Motors are critical components of conveyer belts, elevators, fans, and virtually any electrical device with moving members. Due to the diversity of applications, motor designs have a wide variety of requirements. In some applications, motors with high torque-to-mass ratio or torque-to-volume ratio are desired. For example, motors in NASA probes for outer space explorations and actuators in robotic arms call for low mass and low inertia. In other applications, motors must endure harsh environmental conditions such as extremely high temperatures, requiring the motor material and construction to be rugged.

Currently in the motor industry, induction motors and permanent-magnet (PM) synchronous motors are the predominant motor types because they are relatively easy to control and have decent torque densities. However, they both have their shortcomings. In particular, inductions motors rely on induced currents in the rotor to interact with the magnetic field from the stator. The rotor currents can be very large and generate a lot of heat at low speed. In order to reduce the rotor resistance and thus the amount of heat generated, induction machines have very large and heavy rotors. PM motors, on the other hand, are much more suitable for low or variable speed operations. PM motors, especially the brushless type, are very efficient and reliable. However, the magnets in the rotors are usually made of rare earth elements such as neodymium, or samarium and cobalt, which is a commodity with highly fluctuating prices and limited suppliers. In addition, magnets can potentially be demagnetized by large currents in the stator and harsh environments, especially when the motor is subjected to high temperatures.

This thesis is primarily concerned with the stacked variable-reluctance motor (SVRM), a novel type of variable-reluctance motor (VRM), with parallel air gaps and serial flux. The SVRM was first patented by James H. Goldie and James Kirtley in 1995[3] and 1996 [4]. A SVRM has a plurality of axially interleaving rotors and stators. VRMs in general have much more rugged structures than both induction and PM machines. VRMs have very simple rotors which contain no magnets or squirrel cages. They can stand much higher temperature and they generally exhibit lower rotor inertia. A SVRM in particular has high torque density than a conventional VRM.

The case study on which this project focuses is the construction of a hip motor for the MIT Cheetah Project. The project aims to build a robot resembling a cheetah capable of running at least half as fast as a real cheetah, which can reach 112 kph (70 mph). There are four hip motors that independently control the two rear legs of the robot. The research group is looking for rotary machines that can achieve high torque density with minimum actuator inertia. The basic requirements of the machine are as follows.

- The motor must be less than ⌀120mm × 20mm in size.
- The short term peak heat dissipation of the motor must be less than 2400W.
- Machines with a high torque-to-mass ratio and high torque-to-inertia ratio are preferred.
- The motor must be able to change its speed rapidly. The speed adjustment must be controlled precisely for robot balancing.

1.2 Organization

This thesis is organized into the following chapters.

- Chapter 2 surveys some motor terminology and taxonomy. It presents the concept of the VRM and SVRM, and the benefits of both. It then reviews relevant elementary physics required for later chapters.
- Chapter 3 is the longest chapter of this thesis. It describes the design process of the proposed SVRM. This chapter is divided into four sections. The first

section discusses the topology of the motor, and how to reduce modeling the entire motor to modeling a manageable small rectangular cross-section due to geometric symmetry. The second section describes the material considerations and selection. The third section develops the hybrid computational model that predicts the flux linkage versus current relation of the motor. Using energy conservation, the torque of the motor can be derived from the flux linkage changes. Finally, the forth section presents the Monte Carlo method and the simulated annealing method used for motor geometric optimization and the resulting designs.

- Chapter 4 describes the mechanical design and assembly of a single phase SVRM prototype. Due to the extremely small air gap, material stiffness and bearings selection are considered. In addition, this chapter outlines some difficulties involved in the assembly of the motor and the corresponding solutions.

- Chapter 5 describes the measurements and experiments performed on the prototype. The physical characteristics of the prototype are measured and compared with the mechanical design. Furthermore, the flux linkage and the torque are experimentally determined and compared to the models developed in Chapter 3. All discrepancies found between the model and the experiments are explained and corrected.

- Chapter 6 summarizes the findings of this thesis and proposes future improvements on the SVRM.

1.3 Summary of Conclusions

This thesis shows that the torque performance of a single-phase SVRM prototype matches well with the model developed, after material property corrections. An air gap size of 100 μm in an axial flux motor has been achieved and proven, but it is believed that 50 μm air gaps are also feasible. The maximum measured torque from the prototype with 100 μm air gaps at a 30 A phase current is 2 Nm. The weight of the active material is 0.5 kg. With the same motor dimensions, the models show that a peak torque of 4.29 Nm and an average torque of 1.6 Nm can be achieved at rated 80 A with 50 μm air gaps. Another round of optimization is done using the modified material properties, the best torque-to-mass ratio found for a ferrite motor with no more than 100 pole pairs is 8.4 Nm/kg. It is concluded that ferrite's flux carrying capacity is insufficient for high toque-to-mass ratio motors, given the requirements of the hip motor.

Chapter 2

Fundamentals

This chapter discusses the basic working principles of variable reluctant motors (VRM) and their benefits. It also presents the fundamental physics and the elementary models that will be used later in the thesis to optimize the motor's geometric designs.

2.1 Motor Types

The primary focus of this thesis is to model, design and construct a **stacked variable-reluctance motor (SVRM)** with serial axial flux and multiple parallel air gaps. This section aims to define the above concepts.

In general, a motor consists of a stationary part (stator) and a moving part, separated by a constant gap filled with gas or liquid (air gap). Depending on the type of motor, the moving member exhibits either translational motion (shuttle) or rotational motion (rotor) relative to the stator. The former is called a linear motor and the latter is called a rotational motor. This thesis will focus on the rotational motors.

Among rotational motors, there are two subcategories: radial-flux motors and axial flux motors. Axial motors have magnetic flux lines parallel to the rotor axis of rotation, whereas the radial motors have magnetic flux in the radial direction, orthogonal to the axis of rotation. Figure 2-1 illustrates the difference between these two types of motor. Radial motors are the most common types of motors, and axial

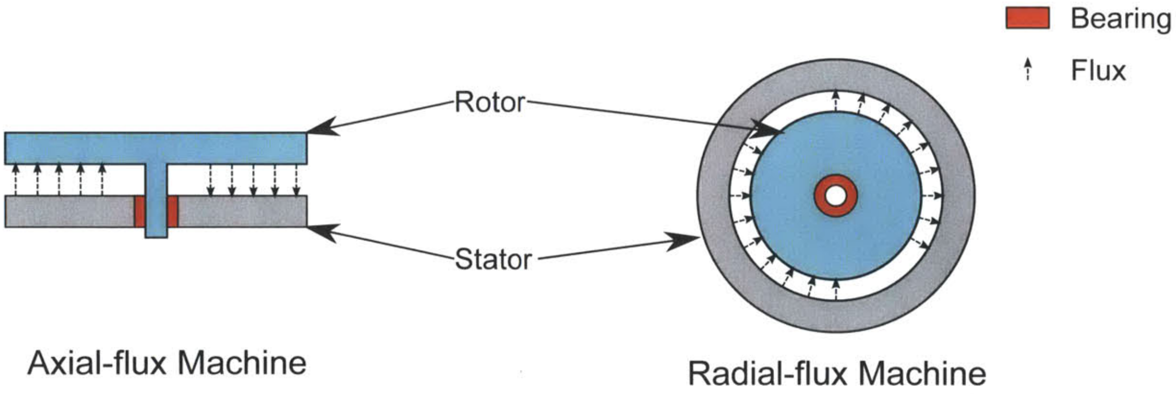

Figure 2-1: Axial-flux machine vs. radial-flux machine

motors remain a hot research topic. The SVRM explored in this thesis has serial axial flux, which means the flux lines traverse through multiple axial air gaps before completing the magnetic loop.

A SVRM is a special type of variable-reluctance motor. It was initially proposed and patented by James Kirtley in 1995 [3] and 1996 [4]. A VRM is also known as a **doubly salient reluctance motor** or a **switched reluctance motor** because it usually requires active current switching for continuous operations. The fundamental principle of a VRM is that when a magnetic field is applied to an unconstrained highly permeable object, the object will rearrange itself into a position that minimizes the total magnetic reluctance experience by the magnetic flux. Magnetic reluctance in a magnetic circuit is the analog of the electrical resistance in an electrical circuit. The torque produced by this principle is called reluctance torque in a motor. The reluctance torque acts to increase the inductance of an excited phase by aligning the stator and rotor poles. This phenomenon was observed in early electrical experiments. The original VRM was invented and patented by W.H. Taylor in as early as 1838, which he named "electromagnetic engine" [5]. However, VRMs were not well researched and adopted until recently largely due to their more costly controller/commutator and its large torque ripples without complex control.

There are three typical rotor positions during an electrical cycle as illustrated in Figure 2-2. The first position, shown in Figure 2-2a, is called the misaligned position,

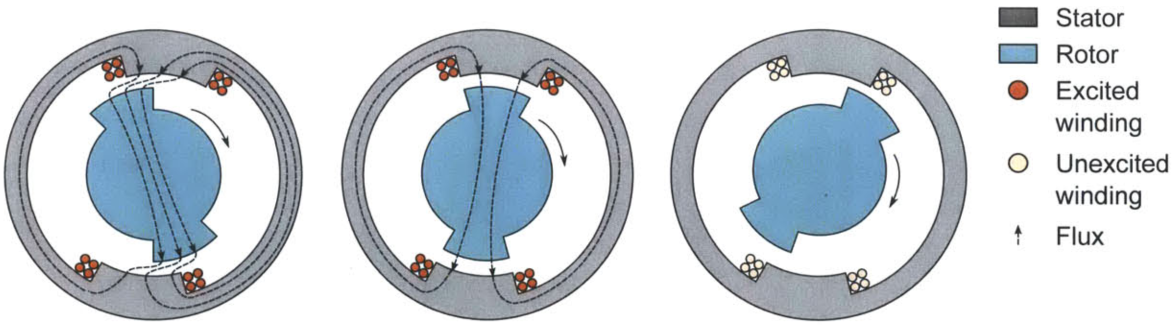

(a)High Reluctance
Low Inductance

(b)Low Reluctance
High Inductance

(c)High Reluctance
Low Inductance

Figure 2-2: (a) Misaligned, (b) aligned and (c) freewheeling rotor positions for a radial VRM.

where the rotor pole is between two stator poles. In this position, the reluctance is large and the inductance is small. When the set coil closest to the rotor poles is excited, the rotor poles try to align themselves with the closest stator poles. In other words, the rotor tries to move to the closest aligned position, shown in Figure 2-2b. The aligned position has the lowest reluctance and the highest inductance. When the stator poles are excited, positive reluctance torque is produced as the rotor moves from a misaligned to an aligned position (from Figure 2-2a to Figure 2-2b); negative reluctance torque is produced when the rotor poles move away from an aligned position. Another way to think about this torque production is that the excited stators poles pull the rotor poles toward them. During continuous operation, the rotor keeps rotating past the aligned position due to its angular momentum; the magnetic field must be switched off during this period. If the coils remain excited, the stator poles will try to pull the rotor back to the old aligned position. When the magnetic field is switched off, no torque is produced and the rotor free wheels until the rotor poles get closer to another set of stator poles. Therefore, the switching of the magnetic field must be synchronous. Since torque is only produced over every other half electrical cycle, torque ripple is hard to avoid, unless sophisticated current profiling is used. Figure 2-3 shows the same three positions for an axial VRM.

Because of the high controller cost and the large torque ripple of VRMs, the indus-

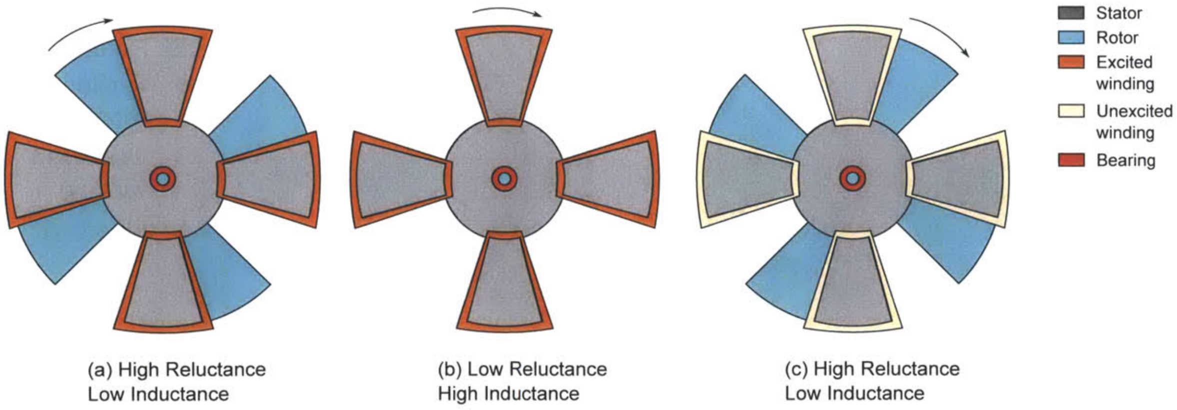
Stator
Rotor
Excited winding
Unexcited winding
Bearing
(a) High Reluctance
Low Inductance
(b) Low Reluctance
High Inductance
(c) High Reluctance
Low Inductance

Figure 2-3: (a) Misaligned, (b) aligned and (c) freewheeling rotor positions for an axial VRM. Back iron is not shown.

try heavily favored AC induction machines and DC machines in the past. However, due to advances in solid state switches and drastic cost reduction of these switches, the cost of controllers is no longer the Achilles' heel of VRMs. The torque ripple of VRMs can also be remedied by advanced motor control schemes. The advantages of the VRM start to shine. These advantages include:

- VRMs contain no brushes, commutators or permanent magnets. Unlike induction motors or DC motors, rotors of VRMs contain no copper or aluminum. Such simplicity not only brings down the cost of manufacturing VRMs, but also means that VRMs are very rugged and easy to maintain. VRMs are suitable for applications with harsh environmental conditions, such as extreme high temperatures.

- VRMs have high top speed because of the simplicity and the ruggedness of the rotors used, which makes them suitable for applications like jet engine generators and high speed spindle drives.

- VRMs operate over a large range of speeds. They do not suffer rotor heating at low speed like inductions motors.

- Because of VRMs' high starting torque and low rotor inertia, they are suitable for applications where quick motor response is required.

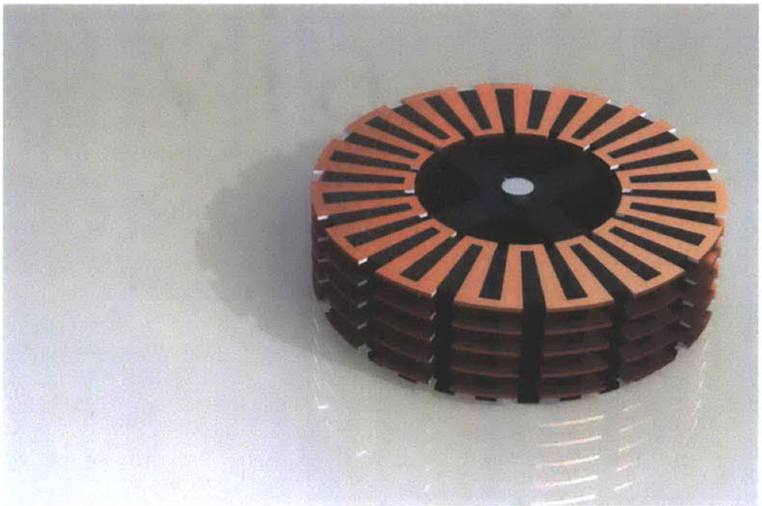

Figure 2-4: Rendering of one SVRM configuration.The blacks parts represent highly permeable core material and the orange parts represent copper wire.

- Heat is generated only in the stator, which is much easier to cool than the rotor because the stator is stationary. Only simple heat management solutions are required. In addition, the stator is generally much larger than the rotor, so the stator can sink a lot more short-term heat generated during peak loads. Consequently, VRMs are very good at dealing with fluctuating loads.
- VRMs have lower apparent power demands than induction and PM motors.

The SVRM investigated in this thesis has multiple parallel rotor/stator interfaces. Figure 2-4 shows one configuration of the motor. The rotors are flat circular disks that contain strips of high permeability material around its outer edge. These radially oriented high permeability strips are the rotor poles. The stators are disks containing stators poles with windings snaking around in between. The stators are sandwiched between layers of rotor disks. See Chapter 3 for a more detailed description of a SVRM.

The novelty of the SVRM design is that the design is very flexible; if more total power or torque is needed, one may simply increase the number the stator/rotor pairs in the axial direction. The total power is roughly linearly proportional to the number of rotor/stator pairs, as long as the power supply to the motor is capable of supplying the required waveforms. The stacked pancake motor is also very efficient at using space. Given a certain volume, the SVRM design offers a much larger active stator and rotor surface area, thus more torque per unit volume.

2.2 Elementary Physics

This section reviews some elementary physical laws and some derived mathematical abstractions. These laws and abstractions will be closely related to the models described in Chapter 3. However, a complete coverage of such information is beyond the scope of this thesis and can be found in relevant textbooks[2][6].

2.2.1 Magnetic Circuit

A typical transformer core with a small air gap in the middle is shown in Figure 2-5. In order to completely define the magnetic behavior of the transformer core, a three-dimensional analysis of the magnetic fields is necessary. However, with some reasonable assumptions and simplifications, this three-dimensional field problem can be turned into a one-dimensional circuit problem with well defined elements. Criteria for magnetic circuit simplification are as follows:

- The problem has to be a magneto-static problem, which means that the size of magnetic object in question is not extremely small and the electrical frequencies involved is not extremely large. This criterion is usually easily fulfilled in a macroscopic magnetic device.

- Magnetic flux has to traverse in a well-defined path. In general, this entails that the magnetic flux is confined in some material with high permeability, and travels across small air gaps where effects of the fringing fields are very small.

- While not necessary, it is generally assumed that the magnetic flux density across a cross-section of the flux path is uniform.

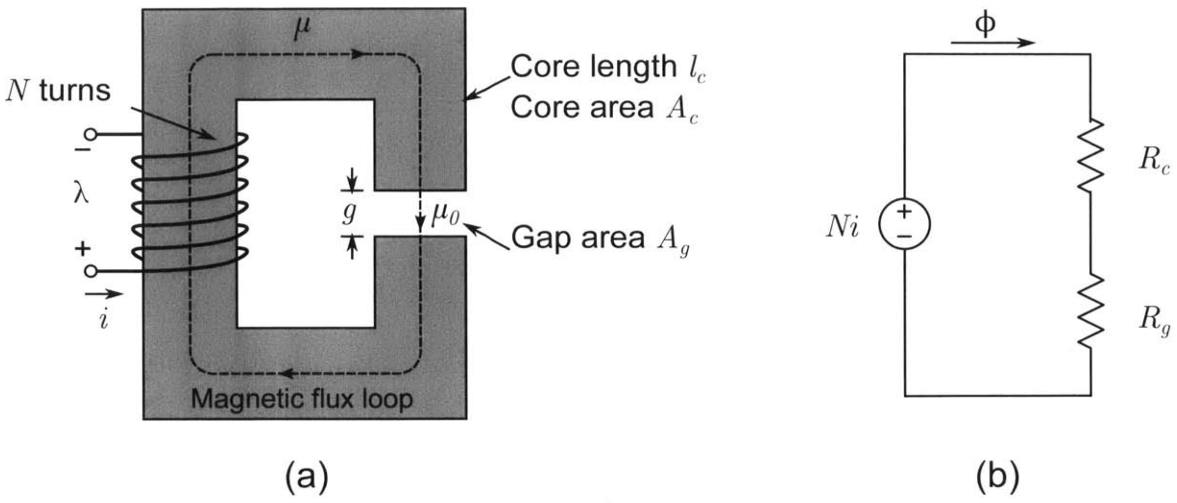
μ
Core length l_c
Core area A_c
N turns
$-$
λ
$+$
i
g
μ_0
Gap area A_g
Magnetic flux loop
(a)
ϕ
R_c
Ni
R_g
(b)

Figure 2-5: (a) C core with air gap, (b) equivalent magnetic circuit.

These criteria are all satisfied in the case of Figure 2-5. Therefore according to the macroscopic Ampere's Law, the magnetomotive force (mmf) $\mathcal{F}$ has the relation

$$\mathcal{F} = Ni = \oint \mathbf{Hdl} \tag{2.1}$$

Since the path and magnitude of the H field are well defined, (2.1) becomes

$$\mathcal{F} = H_c l_c + H_g g \tag{2.2}$$

where H_c and H_g are the mean magnitude of $\mathbf{H}$ in the core and in the gap respectively.

It is assumed that flux is not leaked out of the core and the gap, so the total flux ϕ around the loop stays the same.

$$\begin{aligned} \phi &= B_c A_c = \mu H_c A_c & (2.3) \\ &= B_g A_g = \mu_0 H_g A_g & (2.4) \end{aligned}$$

Combining (2.2)-(2.4), (2.2) can be rewritten as

$$\mathcal{F} = \phi(\mathcal{R}_c + \mathcal{R}_g) \tag{2.5}$$

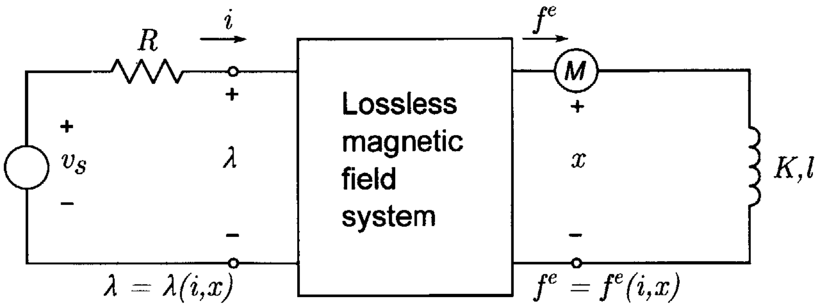

Figure 2-6: Schematic of a lossless magnetic field system. Adapted from [6].

where

$$\mathcal{R}_c = \frac{l_c}{\mu A_c} \tag{2.6}$$

and

$$\mathcal{R}_g = \frac{g}{\mu_0 A_g} \tag{2.7}$$

The relationship between mmf $\mathcal{F}$ and flux ϕ can then represented by a one-dimensional magnetic circuit shown in Figure 2-5b.

2.2.2 Energy and Co-energy

A conservative magnetic system shown in Figure 2-6 converts electrical energy input to mechanical energy output without loss. Note that such an energy conserving system does not include the electrical energy dissipation elements (Resistance R) or mechanical energy storage elements (Mass M). A VRM can be modeled as such a system if the material hysteresis is small. Conservation of energy can be expressed by the equation

$$\frac{dW_m}{dt} = i\frac{d\lambda}{dt} - f^e\frac{dx}{dt} \tag{2.8}$$

The left the side of (2.8) represents the instantaneous rate of change in the energy stored in the magnetic field, which equals the difference between the electrical power put into the system and the mechanical power done by the system, as expressed on the right side.

Multiplying both sides of Equation 2.8 by dt yields

$$dW_m = id\lambda - f^e dx \tag{2.9}$$

Because the magnetic system is conservative, the energy of the magnetic system is path independent and can be described by a scaler function $W_m(\lambda, x)$. Thus,

$$dW_m = \left.\frac{\partial W_m}{\partial \lambda}\right|_x d\lambda + \left.\frac{\partial W_m}{\partial x}\right|_\lambda dx \tag{2.10}$$

Comparison between (2.9) and (2.10) yields

$$f^e = -\left.\frac{\partial W_m(\lambda, x)}{\partial x}\right|_\lambda \tag{2.11}$$

Equation 2.11 relates the electrical force to the energy of the magnetic field. However, expressing energy in terms of λ and x is usually inconvenient; i and x are more natural independent quantities because they are easily measured and controlled. In order to exchange the independent variable λ for i, another state function $W'_m(i, x)$ is introduced. $W'_m(i, x)$ is defined as

$$W'_m = \lambda i - W_m \tag{2.12}$$

W'_m is called the co-energy of the magnetic system and the relationship between W_m and W'_m is shown in Figure 2-7.

Using a Legendre transformation, the electrical force becomes

$$f^e = \frac{\partial W'_m(i, x)}{\partial x} \tag{2.13}$$

If the magnetic material is linear, the co-energy is

$$W'_m = \frac{1}{2} L(x) i^2 \tag{2.14}$$

where $L(x)$ is the inductance and only depends on x. Substituting (2.14) into (2.13)

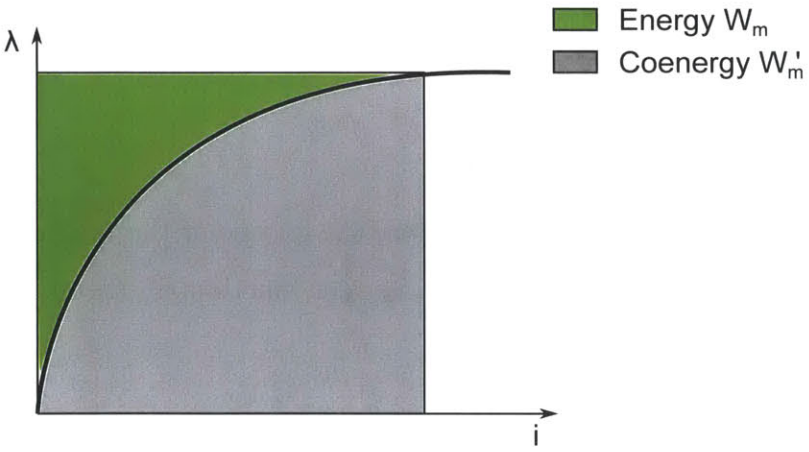

Figure 2-7: Illustration of energy vs coenergy.

yields

$$f^e = \frac{1}{2} i^2 \frac{dL(x)}{dx} \tag{2.15}$$

Equation 2.15 reveals the fact that a larger inductance gradient with respect to position x creates a larger force. Thus, when a VRM is designed, the designer usually tries to maximize the difference between the maximum inductance and minimum inductance experienced by the stator terminals as the rotor spins.

Energy and co-energy methods are effective even if the system is nonlinear, which is usually the case for a VRM operating in the material saturation region. In this case, L is not only a function of x, but also a function of the current i. When this is the case, it is convenient to use energy conservation to calculate the mechanical energy converted. In a cyclical system where the energy in the magnetic field is periodic, the energy in the magnetic field is unchanged over a period. This implies that the mechanical energy converted during that period of time is equal to the electrical energy input. In this case, the integral of the energy and co-energy is the same according to

$$\oint i d\lambda = \oint \lambda di = \oint f^e dx \tag{2.16}$$

Equation 2.16 is graphically illustrated in Figure 2-8.

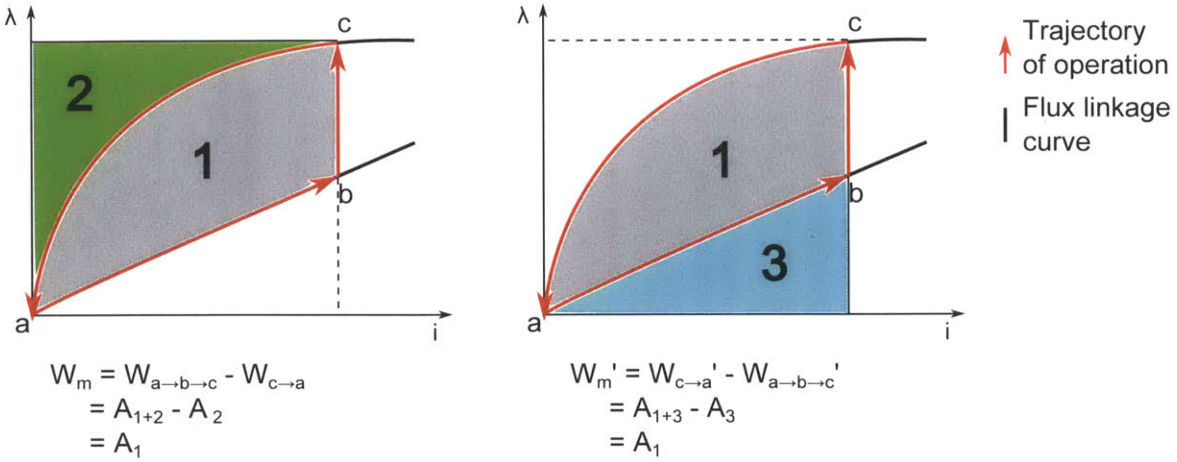
λ
c
2
1
b
a
i
$W_m = W_{a\to b\to c} - W_{c\to a}$
$= A_{1+2} - A_2$
$= A_1$
λ
c
1
b
3
a
i
$W_m' = W_{c\to a}' - W_{a\to b\to c}'$
$= A_{1+3} - A_3$
$= A_1$
Trajectory of operation
Flux linkage curve

Figure 2-8: Comparison between energy and co-energy methods of calculating work done along a trajectory on the $\lambda - i$ plane.

2.3 Summary

This chapter surveyed some terminologies related to SVRM and to motors in general. Potential benefits of the SVRM were presented, including ease of construction, maintenance, and material sourcing. This chapter also reviewed some fundamental physical principles and methods such as the magnetic circuit abstraction and conservative magnetic system abstraction. These basic physical abstractions are heavily used in Chapter 3 to model the magnetic performance of the SVRM.

Chapter 3

Numerical Analysis and Design Optimization

This chapter discusses the characterization and modeling of SVRMs, including material property modeling and motor magnetics modeling. The models are applied to the design process of a robotic cheetah hip motor. A combination of two optimization strategies is carried out, and the results are presented.

3.1 Motor Topology and Model Reduction

The purpose of modeling the magnetics of SVRMs is to predict motor performance, which can be used in optimization processes to find optimal designs across a large geometric design space. Therefore, a good model has to be accurate and efficient. Modeling the SVRM can be complex and slow mainly because of the large number of poles pairs and air gaps. This section discusses the approximations and tradeoffs that are made to model the entire SVRM using only a small, manageable cross-section, which leads to a more efficient geometric optimization process.

The first step towards reducing the motor model is to recognize the symmetry in the motor topology and the magnetic fields. Figure 3-1 is a CAD drawing of the essential functional parts of an SVRM. The SVRM consists of multiple parallel stators and rotors shaped like circular plates. A stator plate is made from a disk of a highly

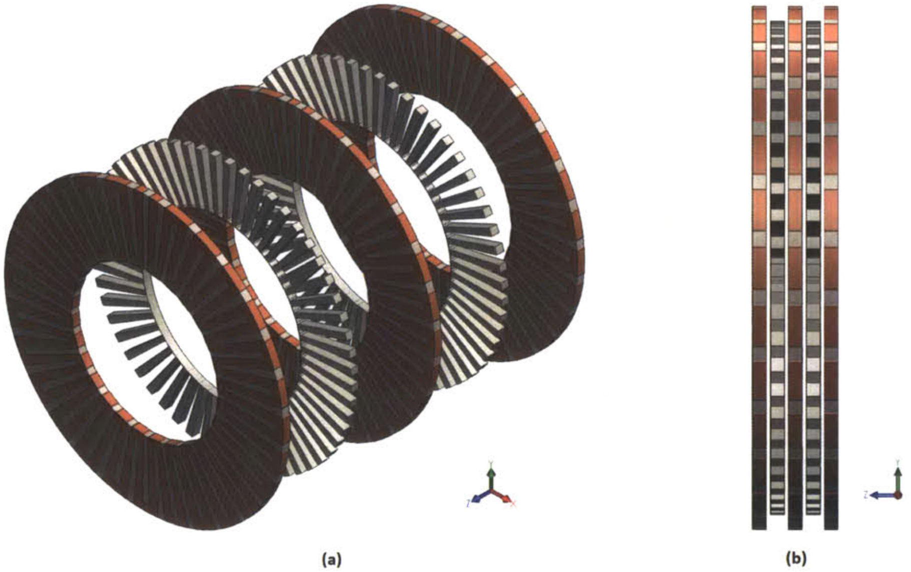

Figure 3-1: 3D drawing of the magnetic elements of SVRM, showing three stator plates and two rotor plates. Air gaps are not drawn to scale for illustration purposes. (a) isometric view (b) x-axis view.

permeable material such as carbon steel or ferrite. Copper wires are embedded in the stator plate, traveling radially in and out around the entire perimeter of the stator plate. A rotor plate has many highly permeable radial spokes, which is also shown in Figure 3-1. Two separate model reductions can be done based on this geometry.

The first model reduction is in the azimuthal direction. When current is driven into the stator winding, magnetic fields are induced in the stator poles perpendicular to the plane of the stator. As the current direction alternates between going towards and away from the center of the stator, the directions of the magnetic fields also alternate between adjacent stator poles, as shown in Figure 3-2. Because the stator poles are equally spaced and the current is the same along a single winding, the magnetic fields exhibit an azimuthal symmetry. Therefore, the model can be reduced to only one stator pole and one part of the copper wire without loss of model accuracy. The resulting segment is highlighted in Figure 3-2.

The second degree of model reduction is in the axial direction. All of the magnetic flux are assumed to be serial, meaning that they must flow through all the stator poles,

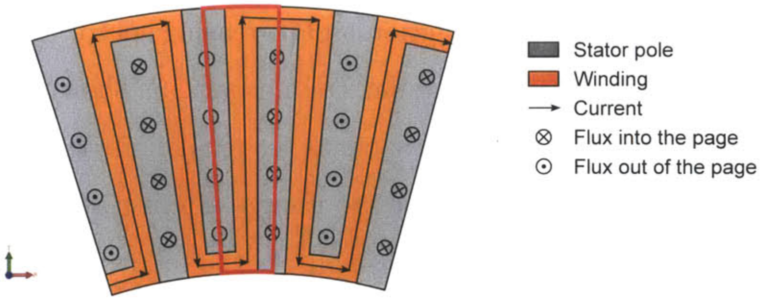

Figure 3-2: Drawing of a section of the stator. The red box highlights one side of the unit cell.

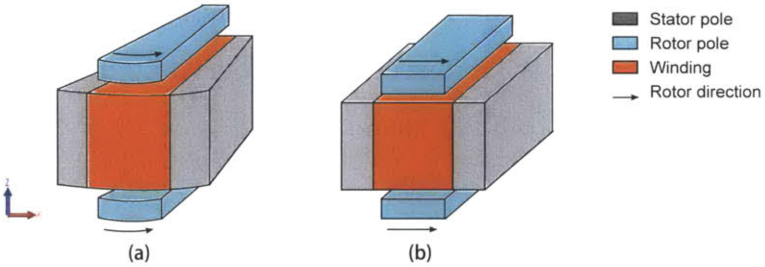

Figure 3-3: 3D drawings of the unit cell. (a) A wedge shaped unit cell. The curvature is exaggerated for illustration purposes. (b) Rectangular approximation of the unit cell.

the air gaps and the back iron plates. Thus, the magnetic flux is conserved across all stator and rotor layers. Furthermore, all stator and rotor layers are geometrically identical and spaced evenly, so the magnetic flux exhibits the same axial periodicity. Therefore, the model can be further reduced to a single stator and a single rotor layer with minimal loss of modeling accuracy. In other words, studying one stator-rotor pair is equivalent to studying all pairs together.

A wedge shaped 3D object emerges after the two model reductions described above. The object (shown in Figure 3-3a) and the magnetics of it are simple enough to be calculated numerically with finite element analysis (FEA). However, the FEA contains very small features, such as the air gap, so it is slow. The resulting optimization processes are too time consuming for a regular workstation at the time of this writing. Therefore, the 3D model is further reduced to a 2D model, forgoing some model accuracy.

For the purpose of simplifying calculation and increasing speed, the wedge shaped 3D object is approximated by a rectangular counterpart, as shown in Figure 3-3b. The width the of the rectangular object is same as the median arc length of the wedge. This approximation works well when there are a large number of pole pairs and the curvature experienced by each pole pair is small. In the following discussion of this thesis, this rectangular model is referred to as the **unit cell**. The unit cell contains one copper segment, two half stator poles, as well as four quarter rotor poles or two half rotor poles, depending on the angle of the rotor in the unit cell. A cross-section of the unit cell in the two different configurations is shown in Figure 3-8. For this rectangular unit cell, studying its cross-section is sufficient to modeling its entirety. Thus, the 3D model is reduced to a 2D model.

3.2 Materials

This section discusses relevant static and dynamic properties of high-permeability materials. Subsection 3.2.1 focuses on the magnetic saturation behavior of different materials, while Subsection 3.2.2 considers magnetic diffusion in the presence of varying magnetic fields within those materials.

3.2.1 Nonlinear Modeling of High-permeability Materials

Because the flux linkage is closely related to the permeability of materials, it is important to precisely predict the permeability of the materials used in the motor. When the material saturation effect is taken into consideration, the magnetic flux in a given material can be expressed as

$$B = \mu(H)H \tag{3.1}$$

where permeability μ is also a function of H.

In general, motor cores are made from steel due to its high permeability. Ferrite is also considered in this thesis because of its low conductivity, which results in fast magnetic diffusion (see more in Subsection 3.2.2). Manufacturers of steel or ferrite

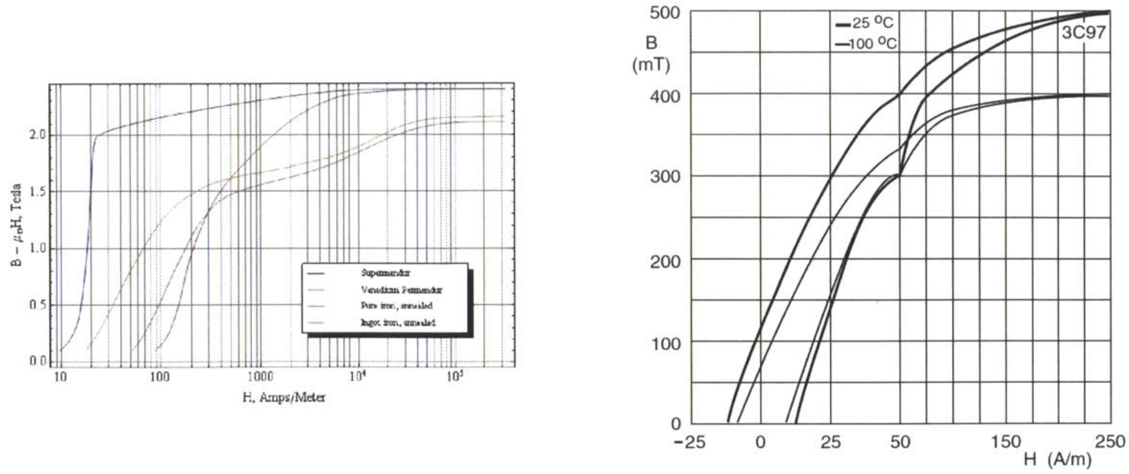

(a)

(b)

Figure 3-4: Typical $B(H)$ curves for (a) steel [1] (b) ferrite 3C97 (Ferroxcube datasheet). Steel has much higher flux carrying capacity than ferrite.

supply the function $\mu(H)$ in some form in their material datasheets. Sometimes, μ is directly plotted against H, and sometimes the $B(H)$ relation is plotted. Figure 3-4 shows some typical $B(H)$ plots from steel and ferrite manufacturers.

There are two shortcomings of such plots. Firstly, the range of these graphs is usually limited. This is especially the case for ferrite because ferrite is often used to construct inductors. Thus, unlike the steel used in reluctance motors, the ferrite in inductors is rarely driven into saturation. In order to get a good torque density in a SVRM, the ferrite used has to be driven well into its saturation region. Secondly, the data from manufacturers is usually a look-up table, which is not suitable for numerical simulation. Due to these two reasons, extrapolations are provided for $\mu(H)$. It is observed from the $\mu(H)$ curves that for a large portion of the graph, except when H is very small, the $\log(H)$ and $\log(\mu)$ are linearly correlated. Thus, the following functions are fitted to the known range of μ values for 3C97 (ferrite from Ferroxcube) and Supermendur (steel [1]), which is expressed as follows.

$$\mu_{supermendur}(H) = 1.575 \times 10^6 (\frac{H}{H_0})^{-0.9811} (H/m) \tag{3.2}$$

$$\mu_{3C97}(H) = 1.854 \times 10^5 (\frac{H}{H_0})^{-0.8614} (H/m) \tag{3.3}$$

where $H_0 = 1\ A/m$. For very small H, μ is assumed to be a constant.

3.2.2 Skin Depth Consideration and Material Selection

When a VRM is excited and rotating, the stator poles experience varying mmf from the windings. If the stator poles are made of conducting materials, the varying mmf causes eddy currents to develop inside the poles. The eddy currents stop the varying magnetic fields from penetrating deeply into the material. Therefore, only the surfaces of the material experience the varying magnetic fields. This phenomenon is known as the skin effect. The skin effect is undesirable for motors because it effectively reduces the useful amount of steel in the motor, and thus reduces the torque produced by the motor. At the same time, the eddy currents produce more heat, which decreases the motor efficiency. Therefore, stator poles of motors, except for coreless motors, are made from steel laminations, which effectively make the steel nonconductive in the direction of the eddy currents. The laminations allow the magnetic field to penetrate into the poles.

The skin depth is used to describe the degree of magnetic field penetration. A small skin depth means the varying magnetic fields only exist on the surfaces of the material. The skin depth for a material with constant permeability μ and conductivity σ is given by [7]

$$\delta = \sqrt{\frac{2}{\omega\sigma\mu}} \tag{3.4}$$

where ω is the angular frequency of the sinusoidal varying mmf. A nonlinear skin effect simulation is executed for this project, because the materials in a SVRM experience heavy saturation and the permeability μ is no longer a constant.

When a current i is driven into the stator winding, it induces a magnetic field B_0 on the side surfaces of the stator poles instantly, as shown in Figure 3-5. Depending on the degree of the skin effect, the time required for this magnetic field to diffuse into the poles differs for different pole materials. The field diffusion satisfies the diffusion

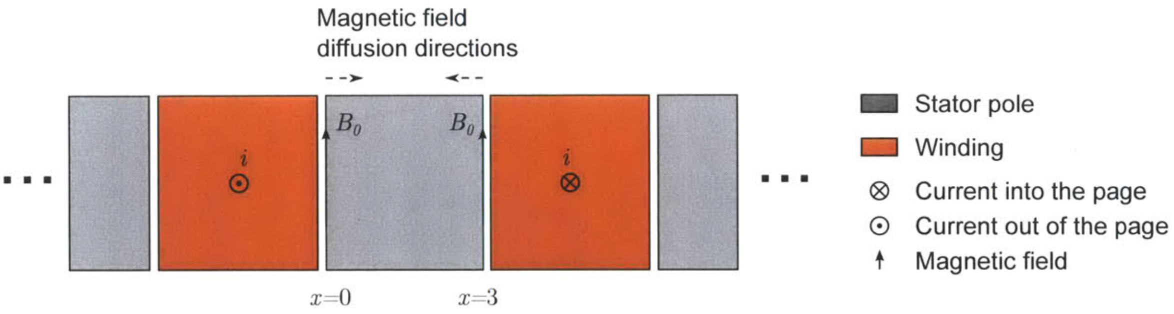
Magnetic field diffusion directions
B0
B0
i
i
x=0
x=3
Stator pole
Winding
Current into the page
Current out of the page
Magnetic field

Figure 3-5: Magnetic diffusion in stator poles.

equation (similar to [7]).

$$\nabla^2 \mathbf{H} = \sigma \frac{\partial \mathbf{B}}{\partial t} \tag{3.5}$$

Since the problem here is a one dimensional problem, the diffusion equation becomes

$$\frac{\partial^2 H}{\partial x^2} = \sigma \frac{\partial B}{\partial t} \tag{3.6}$$

Discretizing (3.6) with time quanta Δt and distance quanta Δx yields

$$\frac{H[\tau, n+1] - 2H[\tau, n] + H[\tau, n-1]}{\Delta x^2} = \sigma \frac{B[\tau+1, n] - B[\tau, n]}{\Delta t} \tag{3.7}$$

Since B and H are related by the material permeability as discussed in Subsection 3.2.1, (3.7) can be rewritten with only B as the unknown using the function $H = \mathcal{H}(B)$:

$$B[\tau+1, n] = B[\tau, n] + \frac{\Delta t}{\sigma \Delta x^2}\{\mathcal{H}(B[\tau, n+1]) - 2\mathcal{H}(B[\tau, n]) + \mathcal{H}(B[\tau, n-1])\} \tag{3.8}$$

The difference equation (3.8) is used to simulate the field diffusion for both Supermendur and 3C97 stator poles. At time $t = 0$, a step B field is applied to both the left and right boundaries of the stator pole. The width of the stator poles is set at 3 mm. The stator poles are assumed to be made of solid steel or solid ferrite, with conductivities of 2.61 MS/m and 0.2 S/m. The resulting magnetic field diffusion is shown in Figure 3-6 and Figure 3-7.

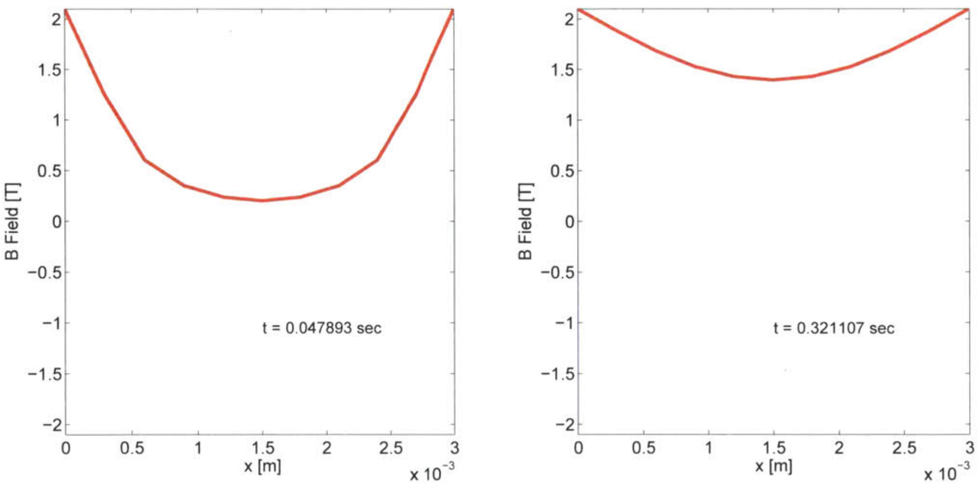

Figure 3-6: Magnetic diffusion simulation results for Supermendur.

The Supermendur plots show that the magnetic field takes half a second to penetrate to the middle. Thus, if the motor is turning at 1000 RPM, there is practically no time for any magnetic diffusion in stator poles. A stator made from Supermendur must be made in laminations to allow magnetic penetration at high RPM. Because the SVRM is an axial motor, the laminations must be cut in concentric cylinders or wedges. Normal axial laminations do not work. However, such laminations are not commercially available at the time of this writing. Therefore, Supermendur, or steel in general, is not suitable for this motor design, unless only static holding torque is required.

On the contrary, the 3C97 plots show that the field only takes on the order of 50 picoseconds for the field to penetrate the 3 mm wide stator poles. This result shows that because ferrite is not conductive, the diffusion is extremely fast. The diffusion rate is actually fast enough to render the skin effect negligible. Therefore, 3C97 ferrite is chosen as the material for the prototype motor.

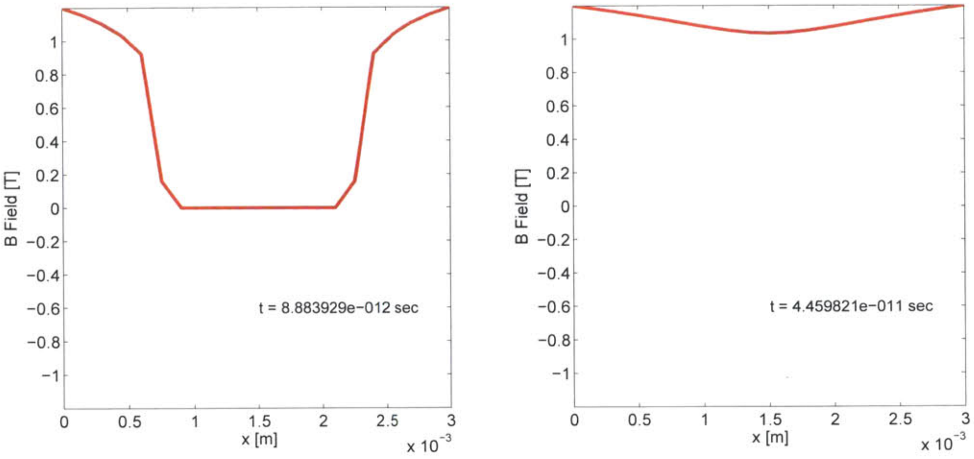

Figure 3-7: Magnetic diffusion simulation results for 3C97.

3.3 Models

The models developed in this chapter estimate the relationship between the terminal magnetic flux linkage and the terminal current in an efficient and accurate way. The torque of the machine can then be calculated using the energy conservation method as discussed in Subsection 2.2.2. When the rotor spins around, the terminal inductance varies periodically. The maximum inductance occurs when the rotor poles are perfectly aligned with the stator poles, as shown in Figure 3-8a. This rotor position is called the **aligned position** or the **maximum inductance position**. The minimum inductance occurs when the rotor poles sit exactly between two stator poles, as shown in Figure 3-8b. This rotor position is called the **unaligned position** or the **minimum inductance position**. Any other positions between the aligned position and unaligned position are referred to as the **misaligned positions**.

3.3.1 Aligned Position (Maximum Inductance) Model

Both analytical and numerical methods can be used to calculate the terminal flux linkage in the aligned position. The analytical method ignores the fringing fields and reduces the magneto-quasistatic field problem to a lumped parameter magnetic circuit model, as discussed in Subsection 2.2.1. The numerical methods uses the finite

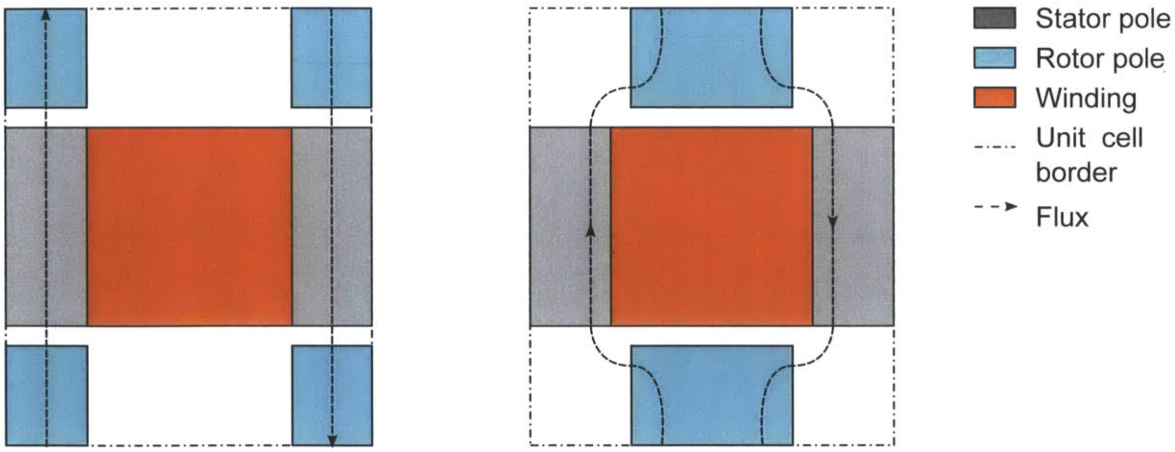

(a) Max Inductance

(b) Min Inductance

Figure 3-8: The unit cell in (a) the maximum inductance and (b) the minimum inductance position.

element analysis software COMSOL Multiphysics to solve the magneto-quasistatic field problem directly.

When the analytic method is used to calculate the magnetic flux linkage, some assumptions are made for the magnetic field. All the fringing fields are ignored because they are very small when the stator and rotor poles are aligned. The mmf drop in the back iron can also be ignored if the back iron is thick and the magnitude of flux in it is small. The magnetic flux travels through the stator and rotor poles and across the air gaps only. In the unit cell shown in Figure 3-9a, the current i driven into the page induces magnetic flux on both sides of the copper winding in opposite directions. Since the mmf drop in the back iron is assumed to be zero, the magnetic circuit only contains the stator reluctance, the rotor reluctance and the air gap reluctance, shown in Figure 3-9b. The magnetic circuit law dictates that the magnetic flux is:

$$\phi = \frac{i}{4R_a + 2R_s + 4R_r} \tag{3.9}$$

where

$$R_a = \frac{g}{\mu_0 A} \tag{3.10}$$

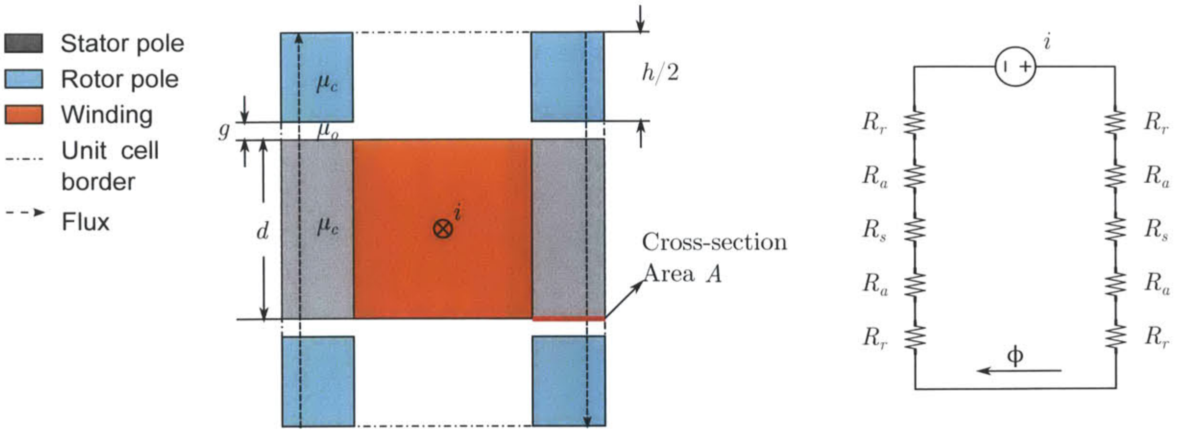
Stator pole
Rotor pole
Winding
Unit cell border
Flux
μ_c
μ_o
μ_c
g
d
$h/2$
i
Cross-section Area A
i
R_r
R_a
R_s
R_a
R_r
R_r
R_a
R_s
R_a
R_r
ϕ

(a) (b)

Figure 3-9: (a) Geometry of the aligned position (b) equivalent magnetic circuit.

$$R_s = \frac{d}{\mu_c(H)\mu_0 A} \tag{3.11}$$

$$R_r = \frac{h/2}{\mu_c(H)\mu_0 A} \tag{3.12}$$

At this point, the number of turns on the winding is assumed to be one. A single-turn winding and a multi-turn winding with the same current density do not differ in their magnetic performance, so there is no loss of generality with this assumption. They only affect the terminal electrical characteristics of machine and the circuit required to drive the machine. The magnetic flux linked by the winding is:

$$\lambda = \phi = \frac{Ai}{\frac{2d}{\mu_c\mu_0} + \frac{2h}{\mu_c\mu_0} + \frac{4g}{\mu_0}} \tag{3.13}$$

Equation 3.13 expresses the magnetic flux linkage λ in terms of the current i, the relative permeability μ_c and other geometric constants. μ_c depends on the stator/rotor materials and the magnetic field intensity H_c in the poles. H_c in the poles is:

$$H_c = \frac{\phi}{\mu_c\mu_0 A} = \frac{i}{2d + 2h + 4g\mu_c} \tag{3.14}$$

Substituting H_c into the nonlinear material model described in Equation 3.3 yields

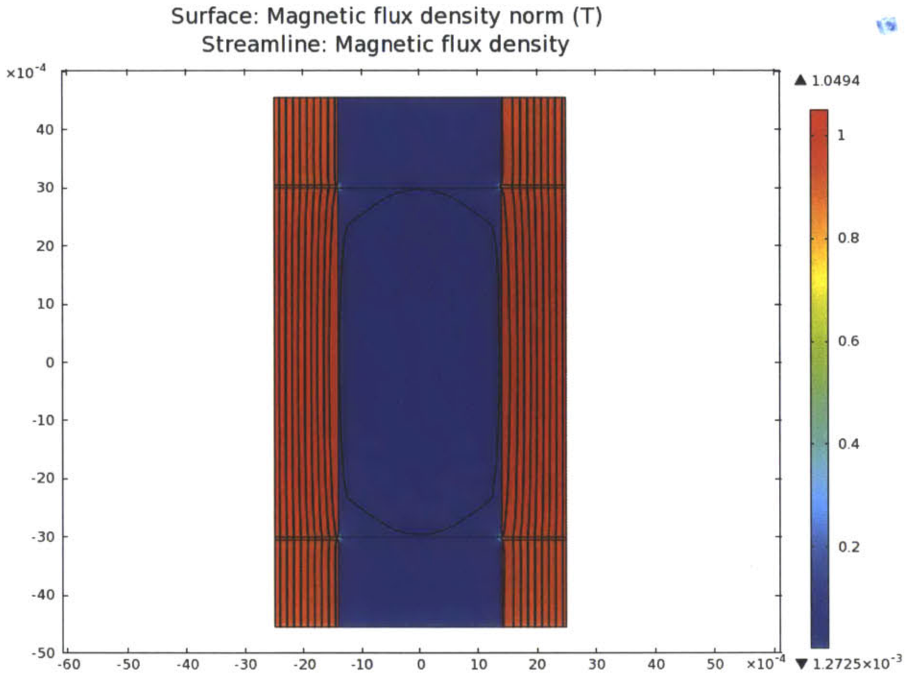

Figure 3-10: FEA field solution of the aligned position. Note the absence of fringing field, as assumed for the analytical model.

the following:

$$\mu_{3C97}(\frac{i}{2d+2h+4g\mu_c}) = \mu_c \tag{3.15}$$

The only unknown here is μ_c, so μ_c can be determined numerically for any terminal current i. With μ_c determined, the magnetic flux linkage λ is easy to find with (3.13). Therefore, when calculating the magnetic flux linkage using the analytical method, the majority of the computing time is spent on solving for μ_c. Since (3.15) only has one unknown, the computing time required is very reasonable.

Magnetic FEA is done using the commercial software COMSOL Multiphysics. The unit cell geometry and the material permeability curves are imported to the software. Boundary conditions are specified, such as continuity for the top and bottom borders and magnetic insulation on the left and right borders. The physics settings involved are Ampere's Law and Single-Turn Coil. Once the above are properly set up in the software, COMSOL is able to solve the field problem. A typical FEA solution is shown in Figure 3-10

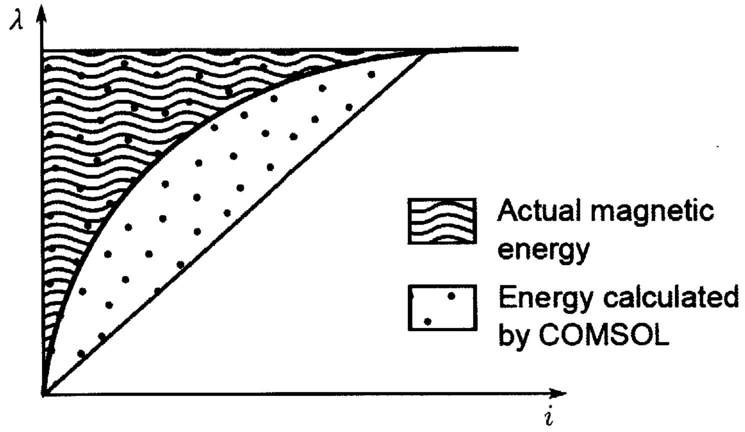

Figure 3-11: Magnetic field energy calculated by COMSOL.

Unfortunately, COMSOL does not generate the flux linkage λ directly, so λ must be derived from some other quantities, such as magnetic flux or magnetic energy. Deriving λ from the total field energy is better because the energy calculation is a volume integral of a scaler field, whereas the flux calculation is a surface integral of a vector field. The flux calculation is further complicated by the fact that the surface integration cannot be carried out over a fixed surface for all rotor angles, while the shape of the unit cell stays the same. One caveat in deriving λ from field energy is that the COMSOL(version 4.2) field energy calculation at the time of this writing is not completely correct. When integrating the field energy, COMSOL assumes the material to be linear, meaning that the integration area on the $\lambda - i$ plane is a simple triangle instead of a more complex nonlinear shape, as shown in Figure 3-11. Therefore, the flux linkage from the energy calculated by COMSOL is

$$\lambda = \frac{2E_{COMSOL}}{i} \tag{3.16}$$

Both the analytic and FEA solutions of the flux linkage versus current curve are plotted in Figure 3-12. As the current increases, the flux linkage increases at the rate of terminal inductance. The terminal inductance is a constant at low current and thus $\lambda(i)$ is nearly linear close to the origin. But when the current increases further and the material gets saturated, the terminal decreases and the flux linkage curve

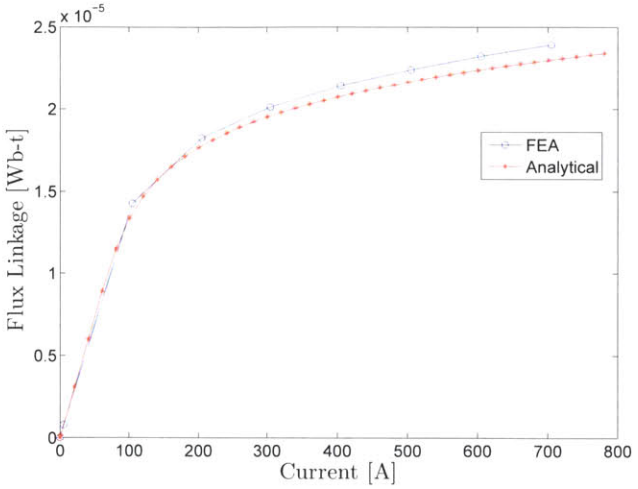

Figure 3-12: $\lambda - i$ curve for the aligned case. The FEA solution and the analytical solutions are very similar. At higher currents, the small difference between the FEA flux linkage and the analytical flux linkage is due to fringing fields.

flattens.

It can be observed that the flux linkage curve from the analytic method is very similar to the FEA solution. It takes 25 seconds on average to obtain the FEA solution with only 8 data points, which is roughly 3 seconds per data point. In contrast, it only takes 0.5 seconds to obtain the analytic solution with 40 data points, which is roughly 0.01 second per data point. In the maximum inductance case, the nonlinear saturation effect is important for energy calculation, so a relatively fine current grid is desired, meaning FEA method will be slow. Thus, the analytical method, with its speed and accuracy, is clearly the superior choice for modeling the aligned position.

3.3.2 Unaligned Position (Minimum Inductance) Model

The inductance of the machine is at a minimum when the rotor poles are in the unaligned position. Because the air gaps are much larger and more irregular, the fringing fields become the dominant factor for the flux linkage modeling. The effect of the fringing fields is highly dependent on the geometry.

Both analytic and numerical methods similar to the maximum inductance case are used to calculate the magnetic flux linkage for the unaligned position. For the analytic

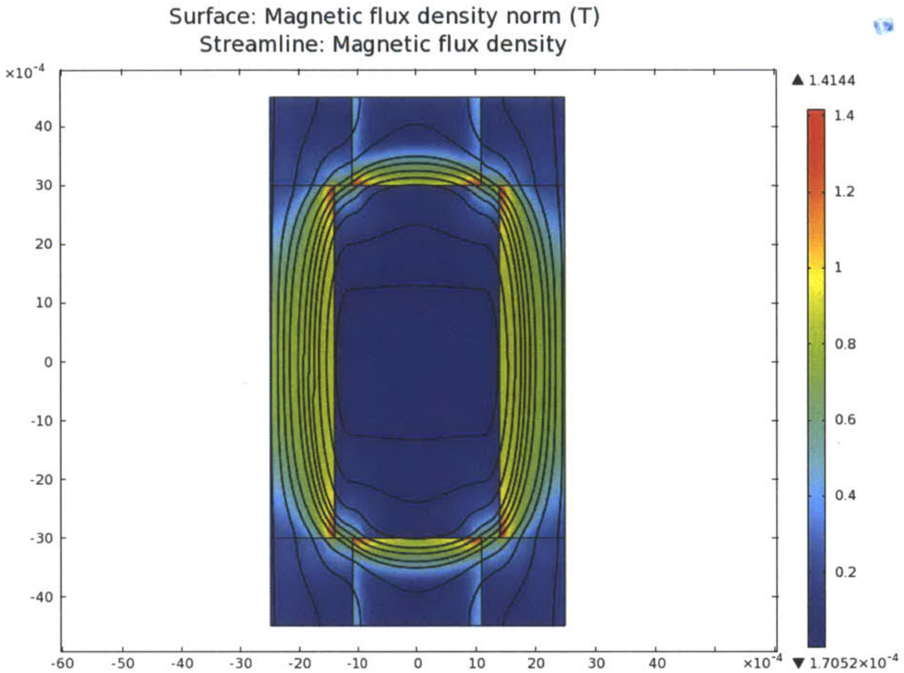

Figure 3-13: FEA field solution of the unaligned position.

model to work correctly, the magnetic flux path has to be accurately predicted and mathematically described. The equivalent magnetic model is a mathematical abstraction of the magnetic flux path, and the accuracy of the circuit is highly dependent on a correctness of the predicted magnetic field path. However, in the unaligned position where the fringing field is dominant, mathematical descriptions of the magnetic flux can usually only be tailored for a specific geometry. A versatile closed-form formula that describes all geometries is difficult to find. Because of the shortcomings of the field descriptions, the analytic model may work well for one geometry in which the flux pattern is well predicted, but may fail for a different geometry because the same flux path prediction may be inaccurate. Thus, the resulting flux linkage calculation will be incorrect for this new geometry. The analytical method is therefore found to be unsuitable to handle the large geometric design space in the optimization process. FEA is believed to be much more accurate in solving the unaligned case and is used as a benchmark for accessing the correctness of the analytic method. One typical FEA solution is shown in Figure 3-13.

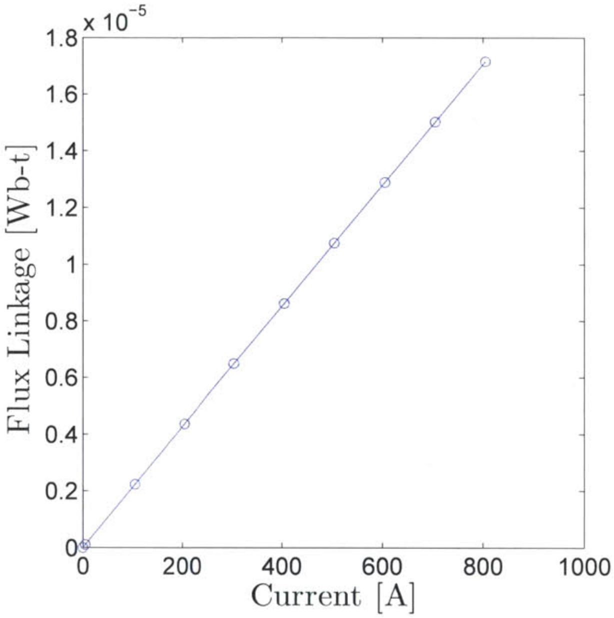

Figure 3-14: $\lambda - i$ curve for the unaligned case.

Due to the above shortcomings of the analytic method, the FEA method is used to model the flux linkage in the unaligned position. One typical $\lambda - i$ curve is shown in Figure 3-14. It can be observed from the graph that the magnetic flux linkage in the unaligned position is linearly proportional to the injected current, as long as the current is not excessively large. This linearity exists because the gap between high permeability materials is much larger, and thus the total magnetic reluctance is dominated by air, which has a constant permeability. This linearity in magnetic flux linkage can be used to dramatically reduce the calculation time, since a single data point can describe the entire magnetic flux linkage curve for the unaligned case.

3.3.3 Total Model

The total model combines the analytical maximum inductance model and the numerical minimum inductance model presented in the previous subsections. Both the maximum magnetic linkage and the minimum magnetic linkage curves are plotted on the same graph, shown in Figure 3-15.

The control scheme used to calculate mechanical energy output is the bang-bang control, due to its simplicity. The terminal voltage is assumed to be infinite. Thus, the current can be changed from zero to i instantaneously at the unaligned angle, and then maintained at i for half an electrical cycle until the rotor rotates to the aligned position. Then the current is turned off instantaneously and kept at zero for the remaining half of the electrical cycle. Such a control scheme accurately simulates an motor with relatively high driving voltage and slow rotational speed. The trajectory of the motor with this control scheme is highlighted in Figure 3-15. The mechanical energy E_e output of the unit cell over an electrical cycle equals to the area enclosed by the loop as discussed in Chapter 2. Therefore, the mechanical power output by the unit cell is:

$$P_{cell} = \frac{E_e}{T_e} \tag{3.17}$$

where T_e is the period of an electrical cycle. If the machine is a three-phase VRM with N_r rotors per phase and N_p pole pairs per rotor, then there are $3N_pN_r$ unit cells in total. Therefore, the total power output of the machine is

$$P_m = 3N_rN_p\frac{E_e}{T_e} \tag{3.18}$$

In a rotary machine, the mechanical power output can also be expressed as

$$P_m = \tau_m * \omega_m = \tau_m * \frac{2\pi}{N_pT_e} \tag{3.19}$$

where τ_m is the motor average torque and ω_m is the mechanical angular frequency of the motor. Subtracting (3.18) from (3.19) yields the torque output of the motor as

$$\tau_m = \frac{3N_rN_p^2E_e}{2\pi} \tag{3.20}$$

To compare the torque performance of different geometric designs, the maximum torque produced by a motor with a given geometry must be calculated using (3.20). N_r and N_p are constants determined by the geometry. Therefore, to maximize the output torque of a given VRM is equivalent to maximizing the energy converted in

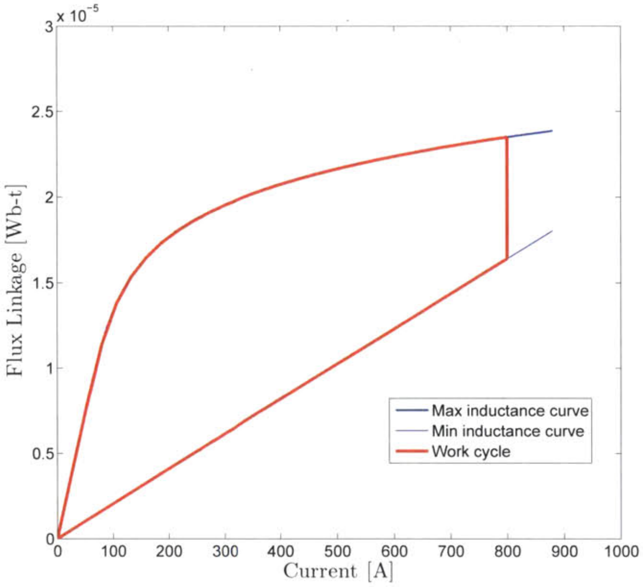

Figure 3-15: $\lambda - i$ trajectory during an electrical cycle.

each cycle. To first order, the maximum torque has nothing to do with the speed of the motor, assuming a power supply is big enough to drive the current waveform. As shown in Figure 3-15, the energy converted in a cycle is determined by the maximum and minimum flux linkages curves and the peak current. The flux linkage is predetermined by the geometry of the given machine and the material of the poles, as modeled in the previous subsections. The current is limited by the thermal performance of the machine. During the maximum torque operation, the ohmic loss is the dominant factor in heat generation. The maximum short-term heat dissipation rate for the cheetah hip motor is 2400 W (Q_{max}).

The average rate of heat generation over an electrical cycle is

$$Q = \frac{1}{2} i^2 R_m \tag{3.21}$$

where R is the total winding resistance of the motor. Therefore, the maximum heat dissipation rate Q_{max} limits the maximum allowed current i_{max} by

$$i_{max} = \sqrt{\frac{2Q_{max}}{R_m}} \tag{3.22}$$

Using the co-energy method, the maximum mechanical energy converted in each electrical cycle is

$$E_{max} = \int_0^{i_{max}} \lambda_{max}(i')di' - \int_0^{i_{max}} \lambda_{min}(i')di' \tag{3.23}$$

Substituting (eq:3-21) into (3.20) yields the maximum average torque for a given motor design.

$$\tau_{max} = \frac{3N_r N_p^2 E_{max}}{2\pi} \tag{3.24}$$

In short, the total magnetics model generates the maximum and minimum inductance curves, while the thermal limit yields the maximum phase current. The energy method combines these two factors and produces the maximum torque for a given geometric design.

3.4 Optimization Processes

Now that a model is established to calculate the maximum torque for a given geometric design, the motor geometry can be optimized numerically. The independent motor geometric parameters to be optimized, as chosen by the author are:

- stator/rotor outer radius;
- stator/rotot inner radius;
- number of pole pairs on the stator;
- ratio of the stator pole width to the copper width;
- stator thickness;
- rotor thickness;

- total motor thickness or the number of rotors per phase.

The geometry of the motor is completely defined by these independent parameters and the air gap size. VRMs with smaller air gaps have better performance. Thus, the study aims to achieve a 50 μm gap. The objective of the optimization process is to find a combination of the above independent variables that results in a motor with the largest torque-to-mass ratio. The most straightforward way to optimize the motor geometry is to carry put a complete grid search over the entire design space. However, this optimization strategy is not selected for several reasons. Firstly, because FEA is used to determine the minimum inductance in the total model, it takes an average of 6 seconds to compute the torque output of any given motor. Thus, it would take an unreasonable amount of time to search through the entire 7-dimensional design space. Secondly, there is an inherent instability in the FEA software COMSOL Multiphysics when it is linked with Matlab. COMSOL would freeze at times. One possible reason for such instability is software memory leaks. Regardless of the reason for the software crashes, manual reset of the software is frequently required.

Given the above constraints, a combination of the Monte Carlo method and the simulated annealing method is used for the motor optimization. The advantage of Monte Carlo is that it scans a large design space well. It is also memoryless, meaning the optimization method does not need to remember what it has done to perform further searches. Therefore, when the FEA program crashes, a new search can be started as if the crash hasn't happened. The simulated annealing method complements Monte Carlo method very nicely. The density of points searched by the Monte Carlo method is arbitrary, meaning it is not very good at finding the maximum, but instead it usually finds points near the maxima. On the contrary, the simulated annealing method is very good at finding a local maximum starting from the proximity of the local maximum. Because these two methods have their advantages and disadvantages, and their advantages complement each other, a combination of the two method is used in this thesis. The Monte Carlo method is initially used to scan large design spaces, and the simulated annealing is used to further refine and improve the Monte Carlo designs.

3.4.1 The Monte Carlo Method

The Monte Carlo method is a simulation algorithm that searches through the design space through random sampling of the geometric design space. The method simply chooses a set of random points in a large and complex design space, and performs a deterministic computation at the each point. For the cheetah hip motor, the computation is carried out for the torque-to-mass ratio. The motor geometry that generates the highest torque-to-mass ratio is then deemed as the "optimal" design in the design space. In general, the Monte Carlo method does not guarantee the best design. Instead, it just offers a good design, or a design that is close to the best design. A more detailed description of the Monte Carlo optimization process used in this thesis is listed in Table 3.1.

Monte Carlo optimization steps
1. Randomly select a point in a given multidimensional geometric design space. 2. Use the model developed in Section 3.3.3 to calculate the torque/mass ratio. Store both the geometric parameters and the simulation results in a separate file. 3. Repeat steps 1-2 until there is decent sample density in the design space. The number of samples required depends on the size of the design space. For this project, it is usually around several thousand samples. 4. Plot torque/mass ratio versus each geometric variable using the data stored in step 2. Find patterns and adjust the design space accordingly, which usually means shrinking the design space to cover only a certain top percentile of the samples. 5. Repeat step 1-4 with the adjusted geometric design space until a satisfactory design is found.

Table 3.1: Steps of the Monte Carlo optimization process

A typical Monte Carlo optimization result is shown in Figure 3-16. In this specific run, roughly 1900 points are evaluated. The torque-to-mass ratio of the machine

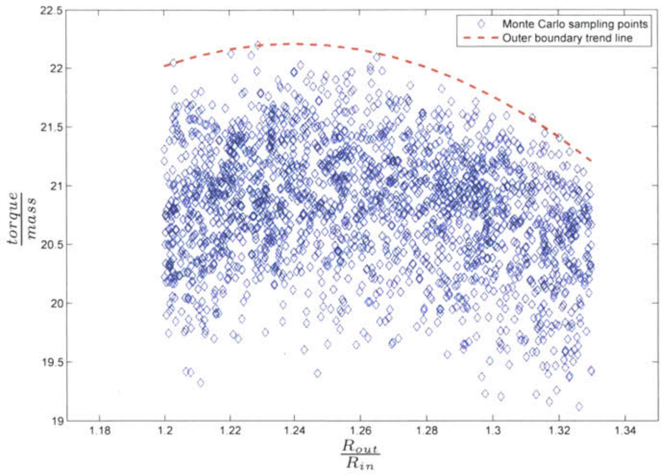

Figure 3-16: Results from a typical Monte Carlo optimization for the motor design. Torque-to-mass ratio is in the units of [Nm/kg].

versus the outer-to-inner stator radius ratio is shown Figure 3-16. The trend line shows the frontier of the performance limit. Based on this trend line, the search space for the radius ratio can be further narrowed to 1.22 to 1.27.

3.4.2 The Simulated Annealing Method

The simulated annealing (SA) method is a probabilistic variant of the deterministic "hill climbing" method. The hill climbing method starts at a point in the design space and evaluates the gradient, i.e. the direction of steepest ascent. It then takes a step in that direction. An appropriate step size guarantees that the move is an "uphill climb". This type of deterministic algorithms is not very suitable for situations where the variables are integers, because it is difficult to combine the gradient with respect to discrete variables and gradient with respect to continuous variables. For example, the number of poles pairs must be a whole number while all other parameters involved in this thesis are continuous. In addition, it is easy for the hill climbing method to dwell on a small hill, or a local maxima.

The SA method remedies these two shortcomings by introducing "random walks" into the deterministic hill climbing method. The simulated annealing method takes a random small step of an arbitrary length towards a random direction from the starting point. Since the gradient calculation is not necessary for the SA method, integer variables are easy to incorporate. The value at the new point is evaluated, and because the step direction is arbitrary, the step could be an uphill climb or a down downhill climb. If the value of the new point is higher (i.e. the step was an uphill climb), the step is automatic accepted. However, in order to escape local maximum traps, a downhill step is also accepted sometimes. This way, the algorithm can walk away from a small hill and towards a larger and higher mountain. The SA method used in this thesis is described in Table 3.2.

Simulated annealing optimization steps
1. Start at a point in a multidimensional design space, with known torque/mass ratio. This is referred to as the *current design.* 2. Randomly alter one of the geometric parameters of the *current design* by a small amount. In other words, find a *perturbed design* from the *current design.* For example, randomly choose a value between ± 10 % of the current value. 3. Compute the torque/mass ratio of the *perturbed design* using the model developed in Section 3.3.3. 4. Compare the torque/mass ratio of the *perturbed design* and the *current design.* • If the new torque/mass ratio is higher, accept the *perturbed design* as the new *current design.* • Otherwise, reject the worse *perturbed design* with probability p, and accept the *perturbed design* as the new *current design* with probably $1-p$. p is usually a predetermined small probability, typically between 0.01 and 0.1. 5. Repeat steps 2-4 until an equilibrium point is reached.

Table 3.2: Steps of the simulated annealing optimization process

All of the designs considered in a typical SA optimization are shown in Figure 3-17, including all the perturbed design. The torque-to-mass ratio of each design is

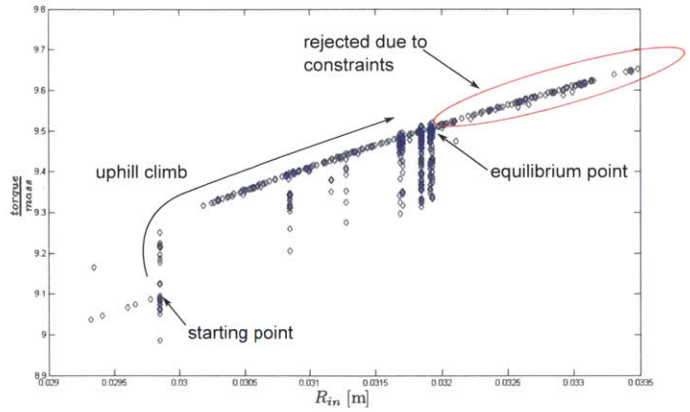

Figure 3-17: A typical result from a SA optimization. Torque-to-mass ratio is in the units of $[Nm/kg]$.

plotted against its rotor inner radius. The SA optimization does mostly an uphill climb from the starting point, until it reached the equilibrium point. Sometimes, the perturbed design would violate some imposed practical design constraints discussed in Subsection 3.4.3, so even though it might have higher torque-to-mass ratio, it is rejected. Such designs are circled in the plot.

One difficulty involved in using the SA method is how to determine what a good maximum step size is and what a good accepting rate p is. When the acceptance rate p is too small, the optimization process gets trapped in local maxima. However, when the acceptance rate is too large, the optimization accepts worse designs too often and wanders off and an equilibrium point would be reached. One way of combatting local maxima is to restart SA from a previous accepted point and sometimes the optimization would go toward a different direction and arrive at a high point. Step size and accepting rate p is experimentally determined.

3.4.3 Optimization Results

Both steel and ferrite are used as candidate materials for the optimization process. The Monte Carlo Method is used to scan the large design space and come up with a good design; the SA method is used then starting from this good design to even better designs. The resulting optimal designs and their performance are shown in Table 3.3. Steel has much higher μ and magnetic flux carrying capacity than ferrite, and thus has much higher torque-to-mass ratio. A steel SVRM is very good at producing a large torque standing still or at low speed. However, steel SVRMs are prone to skin effect at higher RPMs without the correct laminations as discussed in Subsection 3.2.2. Because such laminations are not commercially available at the time of the project, ferrite is chosen to make the prototype and the steel result is only for comparison purposes. Ferrite is a much more difficult material to obtain and machine than steel. Therefore there were several added practical limitations that restricted the prototype design.

- For a motor with a 120 *mm* diameter, it is difficult to fabricate very narrow stator and rotor poles without material cracking. A maximum of 60 pole pairs is imposed on the design.

- The thinnest commercially available ferrite plates have the thickness of 3 *mm*. In order to keep the motor as thin as possible (due to design requirement), all the stators, rotors and back irons are to be made at 3 *mm*.

- The availability of power supplies in the lab restricts the maximum current at $100A$. Each of the two 3 *mm* thick stators has enough thickness to embed five layers of 0.02 inch copper windings. When these winding are connected in series at the end turns, they effectively divide the single turn current in the model by 10. In order to give some headroom for the power supply, the maximum current for the 10-turn copper wire in the design is limited to $80A$, or $800A$ for single-turn winding.

The practical constraints affect the optimization by introducing bounds to the design space. However, it is very easy to apply such constraints to both methods of optimization. The optimization process produces a list of motor designs with high torque-to-mass ratio. One design with relatively low number of pole pairs and high torque density was selected as the prototype design, shown as motor #1 in Table 3.3.

Design number	1	2	3
Material	3C97	3C97	Supermendur
Outer radius [mm]	58.0	57.4	51.7
Inner radius [mm]	30.8	47.0	43.0
Number of pole pairs	56	100	100
Stator width / rotor width	0.78	0.71	0.81
Stator thickness [mm]	6	0.8	2.8
Rotor thickness [mm]	3	1.3	9.6
Number of rotors per phase	1	1	1
Performance			
Maximum current [A]	800	303	539
Torque [Nm]	12.8	1.3	10.5
Torque/weight [Nm/kg]	**9.4**	**8.3**	**35.7**
Torque/volume [Nm/m^3]	3.6×10^4	1.2×10^4	4.0×10^4

Table 3.3: Optimal designs for different materials: (1) 3C97 with practical restrictions; (2) 3C97 without practical restrictions; (3) Supermendur. Note the weight in the torque-to-mass ratio does not involve the weight of motor casing and all other supporting structures. All motors are limited to at most 100 pole pairs.

For comparison purposes, motor #2 is the result of a ferrite motor without any imposed practical restrictions.

3.5 Summary

This chapter discussed the process of geometric model reduction from an entire motor to an simple rectangular cross-section of the unit cell, as well as the tradeoffs of this reduction. Two materials were presented and their skin effect was simulated. Steel, in particular Supermendur, was determined to be not suitable for building SVRMs with large number of pole pairs without proper laminations. A hybrid magnetic model with both analytical method and FEA was shown to be efficient at predicting the magnetic flux linkage and thus the torque output of the motor. The optimization process was also discussed and several optimal designs were compared in Table 3.3.

Chapter 4

Mechanical Design and Fabrication

This chapter describes the process of the mechanical design and fabrication, including the bearing selection, the housing design, and the material stiffness considerations. Problems experienced during fabrication and assembly and their corresponding solutions are also presented.

4.1 Design Objectives

The objective of this mechanical design is to create a prototype that can be used to verify the magnetic models used for motor optimization. The prototype has two 50 μm axial air gaps and the structure must be rigid enough to maintain the air gap under reasonable axial loads. Significant design effort is focused on achieving such an extreme air gap.

4.2 Mechanical Design

4.2.1 Bearing Design

An axial cross-section of the prototype motor design is shown in Figure 4-1. The two stators, the back irons, the bearing housing, and the stator supporting structures are the stationary members of the motor. The axle, the rotor, and the rotor stiffeners are

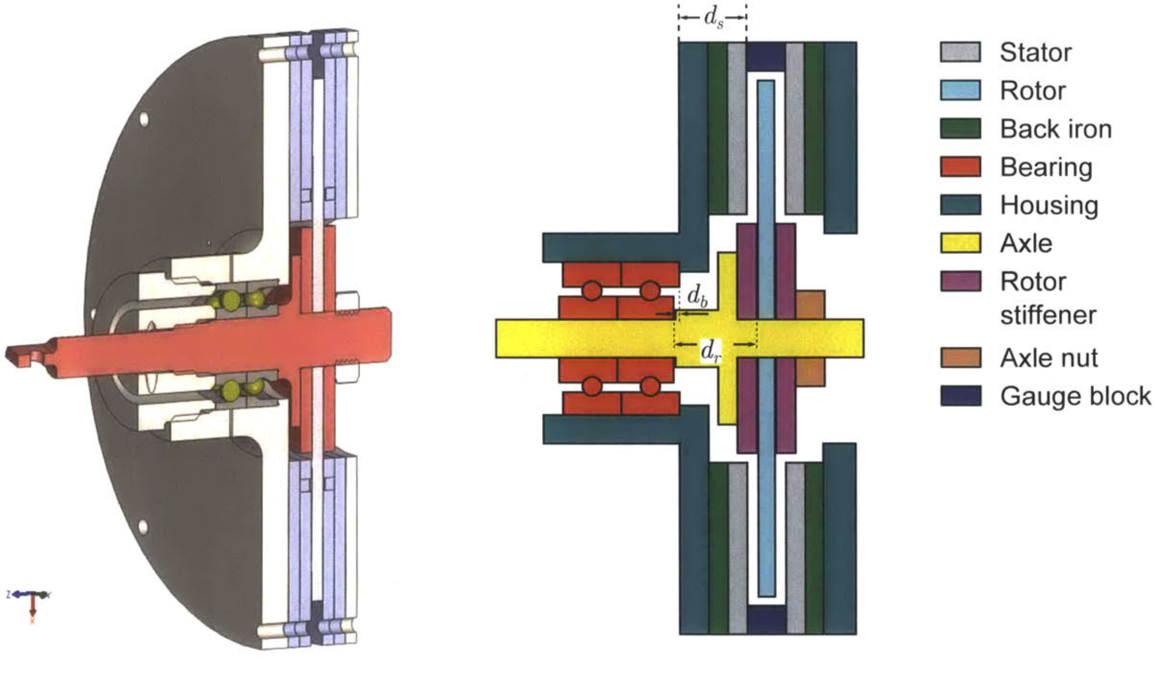

(a) (b)

Figure 4-1: Motor cross-section (a) CAD drawing (b) Schematic with parts labeled with colors.

the rotating members of the motor. Bearings are used to connect the stationary and rotating members. Figure 4-2 shows the exploded view of the motor CAD drawing.

The right stator is mounted to the left stator with a precise gap set by four gauge blocks between them. The thicknesses of the gauge blocks are essentially the same, so the right stator is kept parallel to the left stator. The thickness of the gauge block is the sum of the thickness of the rotor and thicknesses of the two air gaps. As long as the left stator is correctly positioned relative to the rotor, the right stator is as well. Therefore, the following discussion will only focus on the left air gap.

The bearings affect the air gap in three ways. Firstly, when the motor is under no axial load, the axial distance between the inner and outer rings of the right most bearing (d_b) is directly involved in determining the air gap size. The axial distance between the left stator and the outer ring of the right most the bearing (d_s) is the sum the rotor thickness, the back iron thickness and the housing thickness, as shown in Figure 4-1b. The axial distance (d_r) between the rotor and the inner ring of the

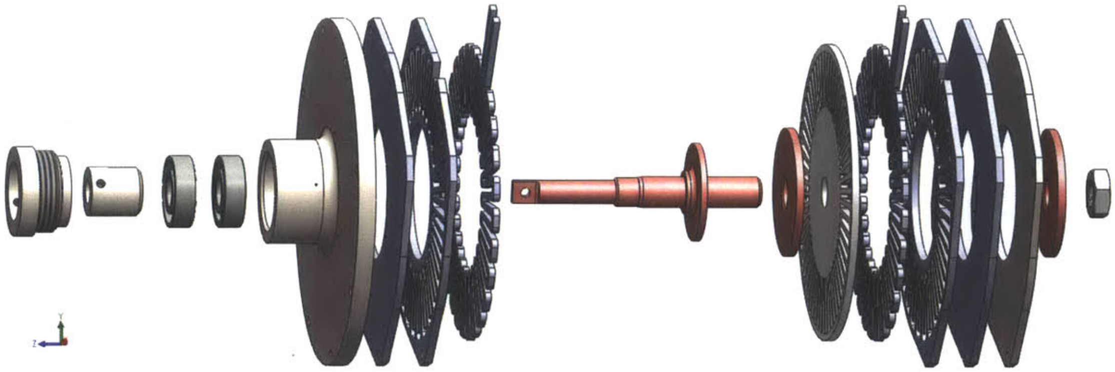

Figure 4-2: Exploded view of the prototype.

right most bearing is determined by the left rotor stiffener thickness and the axle design. The gap size g can be expressed as

$$g = d_r - d_s - d_b \tag{4.1}$$

Among these three distance, d_r and d_s are determined purely by thicknesses of parts and thus can be well specified. In addition, as long as stiff materials are used, these two distance will not change under load. Thus, whether or not the correct air gap can be maintained between the rotor and left stator essentially depends on the distance d_b between bearing rings. d_b for bearings can vary slightly from one to another; d_b also changes slightly depending on the axial preload of the bearing. The variations in d_b, however, can be offset by changing d_r. In other words, the left rotor stiffener acts as a shim that can adjust the no-load air gap. Stiffeners of different thickness are made to compensate for the variations in d_b.

Secondly, when the motor is turned on, there is some axial load on the rotor. In order to maintain the air gap, d_b should stay the same or change very little under axial load. The change in d_b is closely related to the axial rigidity of the bearing, which is determined by the type of bearings used and the axial preload of the bearings. A set of back-to-back mounted ultra-precision angular-contact bearings is selected because the axial stiffness of such a bearing configuration is exceptional. The bearing surfaces

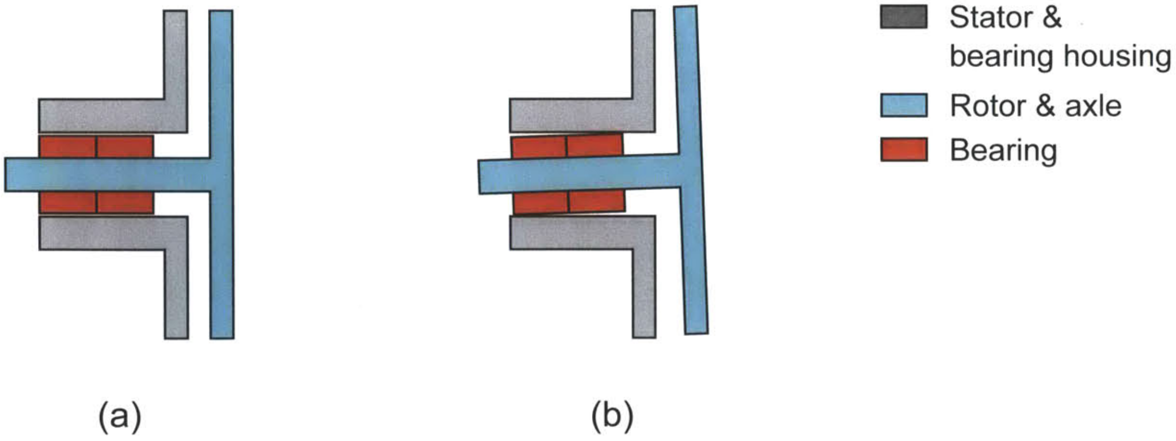

Figure 4-3: (a) The perfect and (b) the most misaligned position for the rotor.

are precision ground so when they are mounted in pairs, a preload is automatically applied to axially stiffen the bearing set. Two SKF 7001 CDGA/P4A bearings are purchased from mcmaster.com.

Lastly, the bearings also affect the air gap by how they fit within the bearing housing. In this case, the the inner ring is rotating and the outer ring is stationary, so an interference fit between the axle and inner ring is recommended by the bearing manufacturer SKF, as well as a clearance fit between the outer ring and the housing. The shaft is designed with a 2.5 μm interference fit. In other words, the axle diameter is designed to be 2.5 μm larger than the ID of the bearings.

A clearance fit, or slip fit, is recommended between the outer ring and the housing. This means the ID of the housing is larger than the OD of the bearings. The extra radial clearance means can the axle can sit in the housing with a misalignment angle or a cocking angle, as shown in Figure 4-3. However, A typical clearance fit value suggested by the bearing manufacturer is too loose. It creates a misalignment angle that is too large to be suitable for this application, and thus the axial displacement at the tip of the rotor will also be too large. An excessive tip wobble of the rotor causes the rotor to run into the stator. The misalignment angle and redial clearance must be carefully calculated.

The geometry of the worst bearing misalignment angle and the resulting axial displacement or axial wobble of the rotor tip is illustrated in Figure 4-4 . The rela-

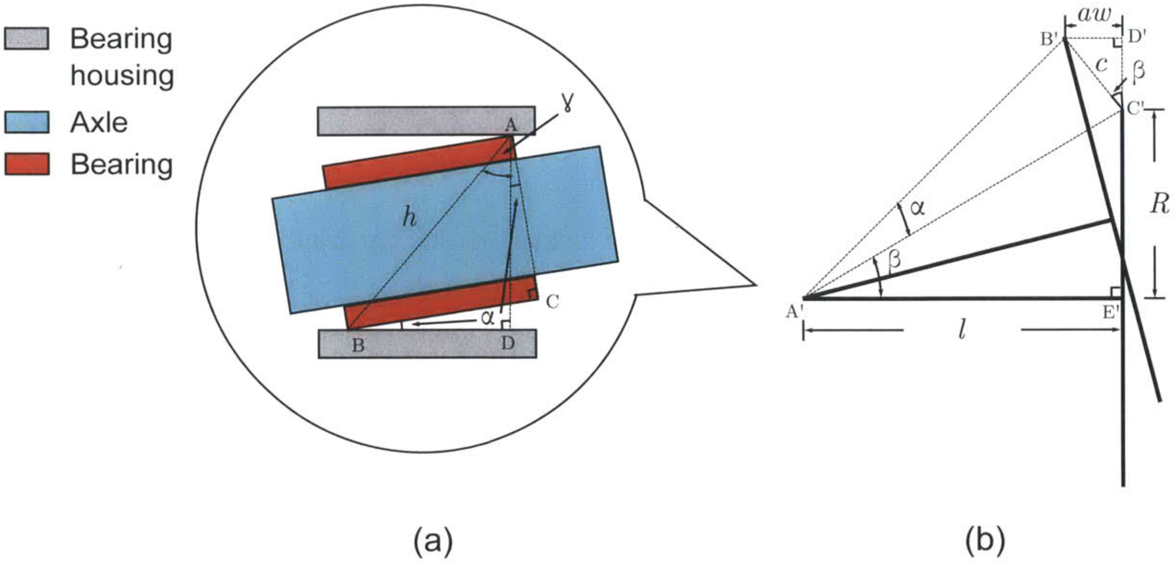

Figure 4-4: (a) zoomed-in view and the geometry of the bearing fitting and (b) the resulting geometry of the axle/rotor misalignment. The two large bold T's in the schematic represent the two axle/rotor positions shown in Figure 4-3.

tionship between the rotor tip axial displacement (a_w) and the radial clearance (r_c) can be calculated using trigonometry as follows.

Figure 4-4a is a zoomed-in view of how bearings fit in the housing with some radial clearance. $\triangle ABC$ and $\triangle ABD$ are both right triangles and thus

$$\cos(\alpha + \gamma) = \frac{|AC|}{|AB|} = \frac{d_o}{h} \tag{4.2}$$

$$\cos(\gamma) = \frac{|AD|}{|AB|} = \frac{d_o + 2r_c}{h} \tag{4.3}$$

where d_o is the bearing OD, and r_c is the radial clearance of the bearing housing. h is the distance between the opposite corners of the two outer most bearings in a N-bearing mounting configuration. If b_w is the width of each bearing, h can be expressed as

$$h = \sqrt{(d_o + 2r_c)^2 + (Nb_w)^2} \tag{4.4}$$

Axle misalignment angle α can be then calculated from (4.2) and (4.3)

$$\alpha = \arccos(\frac{d_o}{h}) - \arccos(\frac{d_o + 2r_c}{h}) \tag{4.5}$$

Once the the axle misalignment angle α is known, the tip axial displacement (a_w) of the rotor can also be calculated. Figure 4-4 shows the effect of misalignment angle on the axle and rotor. The two bold T's represent the rotor in the perfect and the most misaligned positions. Because $\triangle A'B'C'$ is an isosceles triangle, c can be expressed as

$$c = 2\sqrt{R^2 + l^2} \sin \frac{\alpha}{2} \tag{4.6}$$

When the misalignment angle α is small, small angle sine approximation yields,

$$c \approx \sqrt{R^2 + l^2}\alpha \tag{4.7}$$

Since c is the length of the hypotenuse in the right triangle $B'C'D'$, the axial displacement a_w is

$$\begin{aligned} a_w &= c \cdot \sin \beta && (4.8) \\ &= \sqrt{R^2 + l^2}\alpha \sin \beta && (4.9) \end{aligned}$$

where

$$\beta = \arctan(\frac{R}{l}) \tag{4.10}$$

The combination of (4.5) and (4.9) relates the radial clearance r_c and number of bearings N to the axial wobble a_w. The relevant equations are entered into a spreadsheet and different radial clearances and numbers of bearings are experimented with. Thus, the smaller the radial clearance is the smaller the axial wobble is. A radial clearance of 0.0025 mm is chosen based on the limitation in machining tolerance. With two bearings at 0.0025 mm radial clearance, the maximum axial displacement is 19 μm, which is acceptable. In addition, the outer bearing retainer that holds the bearings in place also helps align the bearings.

4.2.2 Rotor Stiffness

When the rotor sits directly in the middle of the adjacent stators, the net axial force on it is zero. However, when the rotor is offset a tiny bit axially, the magnetic force experienced by the rotor is in the direction that makes the offset larger. This phenomenon is called the negative stiffness of the motor. This negative stiffness must be overcome by the positive stiffness of the rotor. The positive stiffness of the rotor depends on the material and the geometry of the rotor.

The rotor is made of ferrite due to its magnetic properties and low conductivity as discussed in Subsection 3.2.2. Among different types of ferrite, the ones with high flux carrying capacity are preferred, but the ferrite also must be stiff enough to resist the negative stiffness. Many ferrite manufacturers and distributors are contacted. Among the companies contacted, only Elna Magnets has ferrite plates available in the appropriate dimensions (at least $120mm \times 120mm$). The ferrite plates are made of material 3C97 from Ferroxcube.

One of the most important geometric dimensions that affects the stiffness of a circular plate is the thickness. 3C97 plates 3 mm are the thinnest available from Elna Magnets. It is chosen because of the motor thickness requirement. Deflection FEA is performed on the rotor design to verify that the stiffness of 3C97 at 3 mm is sufficient to compensate for the negative stiffness of the motor. In addition, the stress on the material must be lower than the material yield strength.

In order to find the negative stiffness of the motor, the rotor is offset to one side by 10 μm and the resulting axial force is calculated. Magnetics FEA is performed on the unit cell using COMSOL Multiphysics at different angles across an electrical cycle. Figure 4-5 shows the rotational torque and axial force the rotor experiences at the 10 μm offset. The peak torque acts upon a single rotor is 13.08 Nm and the peak axial force is 39.8 N at this offset.

Then a deflection FEA is performed using the built-in simulation function of Solidworks. The relevant material properties are the Young's modulus and ultimate

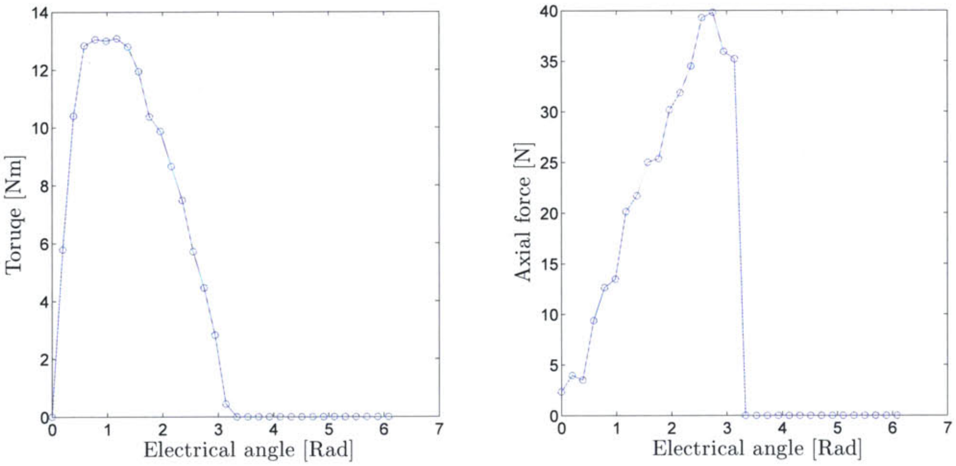

Figure 4-5: Torque and axial force experienced by the a single rotor over an electrical cycle. The values are calculated directly using FEA for the prototype. The FEA average torque is very similar to what the theory predicts (See Chapter 5 for details of the comparison).

tensile/compressive strength of ferrite. The rotor is assumed to be fixed around the perimeter of the rotor stiffener, and the peak rotational torque and the peak axial force found above are applied on the rotor poles. Figure 4-6 shows the resulting Z displacement and Von Mises stress. The maximum expected axial deflection is $5.584\mu m$, which means the rotor's stiffness is higher than the negative stiffness of the machine. Also, the maximum stress experienced by the ferrite is smaller than the average ultimate strength, which means the average rotor can withstand the force without breaking.

4.3 Fabrication Processes

4.3.1 Stator, Rotor, Back Iron and Winding

The stators, the rotor and the back irons are made of ferrite. The ferrite stock comes in as 120 $mm\times$ 120 $mm\times$ 3 mm plates. From the cross-section shown in Figure 4-1, it is apparent that in order for the small air gap to work, all the ferrite pieces involved must be extremely flat. All plates received are inspected with a coordinate measuring

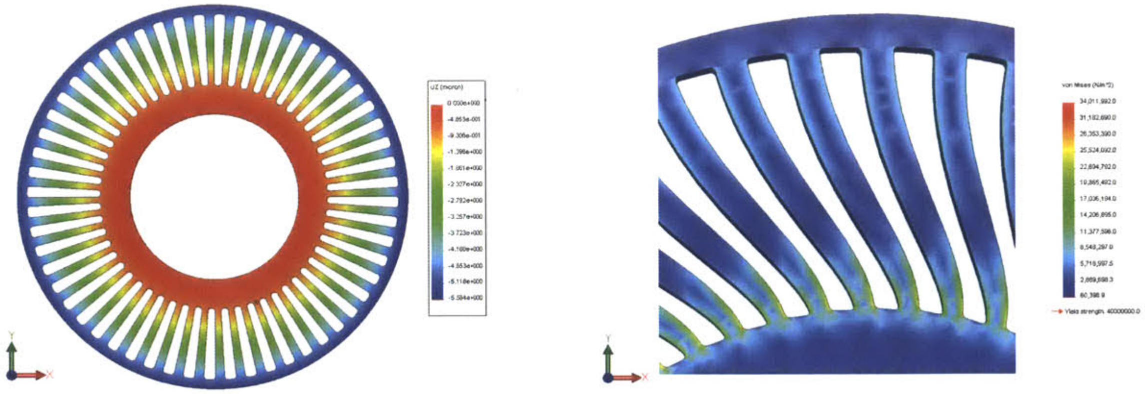

(a)

(b)

Figure 4-6: (a)Maximum z displacement (b) Maximum stress experience by the rotor. The deformation is exaggerated for illustration purposes.

machine (CMM). The plates are positioned flat on a granite table and the height of both sides are measured along a probing path. The results from one plate are shown in Figure 4-7. Among the ten plates ordered, two of them have flatness larger than 20 μm and are rejected.

Due to the small design feature size and the two dimensional design pattern, it is most effective to cut the ferrite stock with a water jet. The water jet used is an Omax Jet Machine Center from the MIT Hobby Shop. Because no one has prior experience in cutting MnZn ferrite at the site, test cuts are performed on the material and the following settings are ultimately used.

Setting Name	**Selection**
Machinability	50
Brittle material	checked
Low pressure piercing	checked

Table 4.1: Settings used in water jetting 3C97 ferrite

As suggested by Omax to estimate the machinability number of ferrite,

$$Machinablity = (\frac{1919}{RB})^{1.4474} \tag{4.11}$$

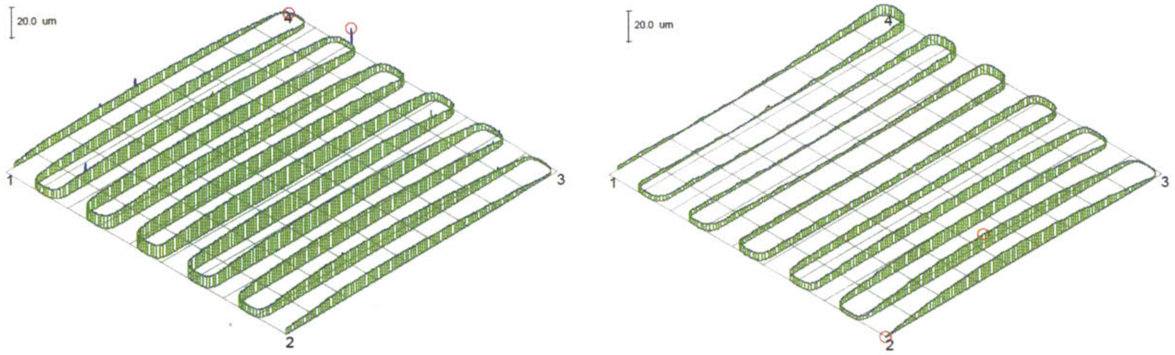

(a) (b)

Figure 4-7: The flatness measurement of two sides of a 3C97 plate.

where RB is the Rockwell B hardness. The Vicker hardness of 3C97 is between 600-700 N/mm^2 and thus the machinability is around 50. Test cuts confirm this calculation.

3C97, like most ferrites, it is very brittle. The brittleness of ferrite is a double-edged sword. On one hand, because of the brittleness, there are no burrs around the cutting edges. It is extremely helpful for this project because it would be very difficult to deburr the stator and rotor pieces after cutting. When trial stator pieces are made from aluminum, deburring is done through surface sanding. However, it would have been very difficult to sand the stator surface down without affecting the flatness or parallelism of the ferrite plates. Precision grinding machines would have been needed. On the other hand, the brittleness of the ferrite also causes considerable cracking problems during fabrication.

When a water jet is used to make small parts, a piece of large stock material is usually laid on a waterjet brick and secured with weights. A waterjet brick is a piece of corrugated plastic with vertical channels to allow the jet to flow and avoid jet splash back. Because waterjet bricks wear very fast and unevenly, it is very easy for the stock plate to be supported unevenly. When the stock material is not well

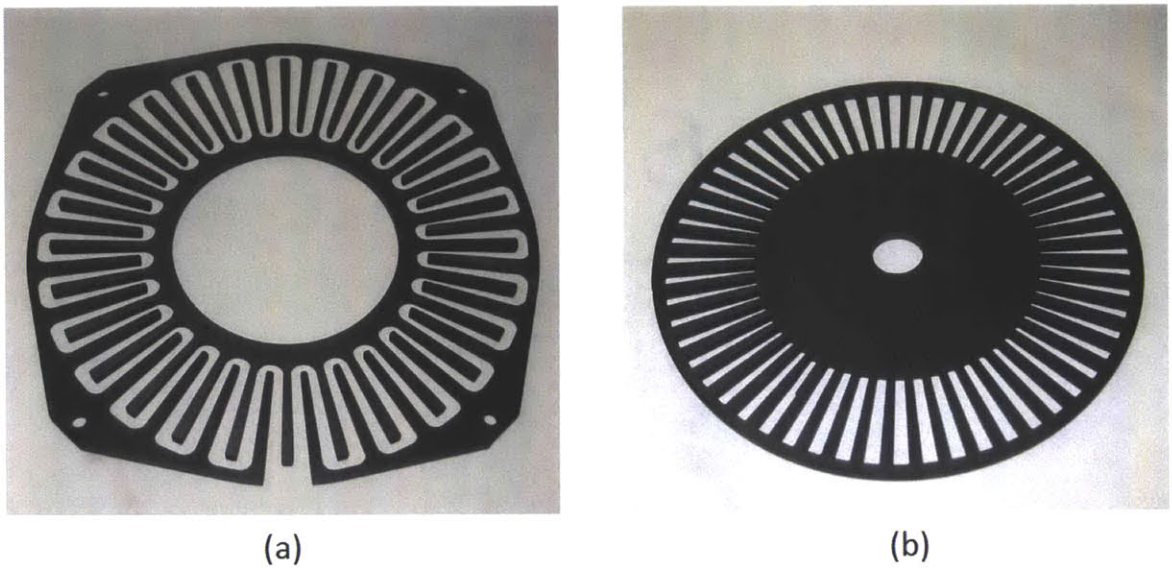
(a) (b)

Figure 4-8: (a)Stator and (b)rotor after water jet cutting.

supported, the cutting stress cannot be transferred to the supporting brick well and stress is built up in the stock instead. The localized cutting stress is large enough in ferrite that the small features on the stator design keeps cracking during cutting. This problem is solved by using a 1/8 inch aluminum sheet as an additional back support. The ferrite plates are taped to the aluminum backing with 3M Paper Tape 401M at four corners. The water jet cuts the aluminum backing and the ferrite plate at the same time. This type of configuration, however, introduces splash back during initial piercing. When the jet is used to drill a hole, the jet first pierces through the top material. Then, when it is piercing through the bottom material, water and abrasives splash back up and change the size of the hole drilled for the top material. This phenomenon is especially obvious when drilling small holes. The splash back problem is solved by pre-drilling oversized holes at the identical locations on the bottom aluminum support before ferrite plates are taped on. This way, there is no splash back because there is no backing materials where a hole is drilled on the top. The cut stator and rotor pieces are shown in Figure 4-8.

Copper windings are cut from 0.02 inch pure copper sheets using the same water jet. The cut pieces are surface sanded by hand to deburr the edges. Parylene coating

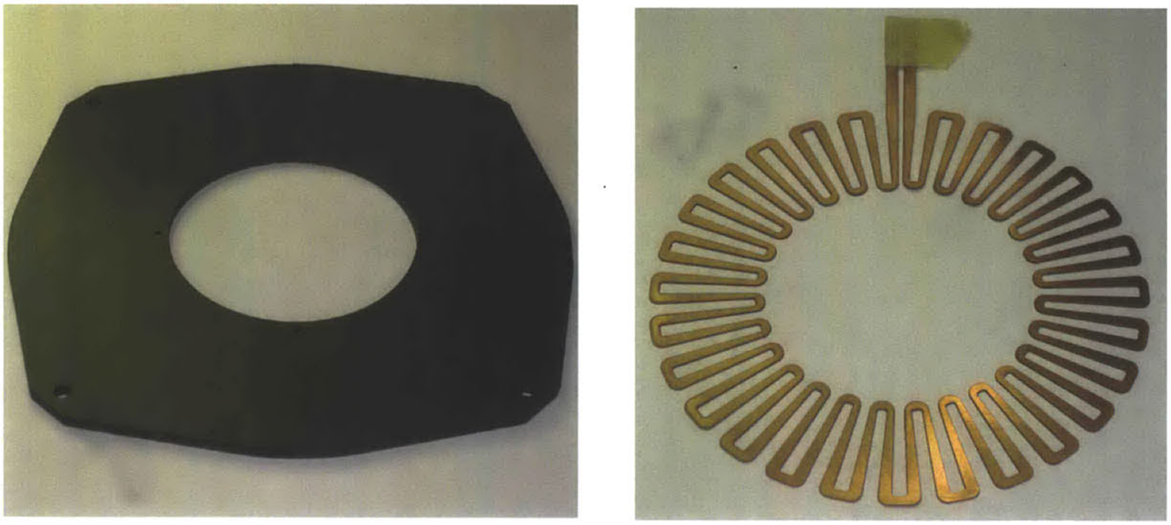

(a) (b)

Figure 4-9: (a)Back iron plate (b)copper wingding with terminal masking.

is used as insulation between adjacent layers of copper windings. Copper windings are masked at the leads and hung on a rotating platform during coating. A total thickness of 10 μm thick of parylene is evenly deposited on all surfaces in two separate 5 μm coating runs. The resulting copper winding is shown in Figure 4-9b.

4.3.2 Supporting Structure

All supporting structures for the prototype are made from grade 304 austenitic steel, except the axle, which is made from 17-4 PH stainless steel for its hardness. The austenitic steel is chosen so that the supporting structure does not interfere with the magnetics of the motor. The objective of this design decision is to separate the mechanical supporting design from the motor magnetic design, so that these two aspects of the motor can be separately evaluated. However, it is not inconceivable for more aggressive weight saving strategies to be implemented, wherein the supporting structure also acts as the back iron. The axle must be harder to take loads without excessive flexing. The axle is far enough away from the stators/rotors that it does not interfere the magnetic flux loop.

Due to the tolerances needed, all the supporting structures are not made in house.

The supporting structures are machined by Kal Machining Inc. All the mechanical drawings are attached in Appendix A. GD&T is used to specify crucial geometric features.

4.3.3 Assembly

Compared to the fabrication of the parts, the assembly process is fairly fast and painless. The assembly is done in house. Special attentions are paid to maintain the flatness of the stator layers.

First, the back iron and the stator layers must be mounted to the supporting structures. It is crucial that the distance between the different layers be as small as possible because these gaps are in the direct path of the motor magnetic path. It is equally important that the layers are glued parallel to each other. Air bubbles in the adhesive between layers can cause the stator to be slanted and thus rub against the rotor. Advanced adhesive coating technique such as spin coating can be used to achieve an very thin and bubble-free layer of adhesive. However, such a coating machine is not accessible during the assembly.

The alternative solution is to avoid adhesives all together between the back iron and the stator layers. Instead, epoxy is applied to all the seams. Laminating Epoxy 105/206 combo from West Systems is selected because of its low viscosity and long working time. $3-5\%$ acetone by volume is then added to the epoxy mixture as a thinner. The acetone also extends the working time but slightly reduces the strength of the cured epoxy. The epoxy mixture is very carefully applied with a thin tip syringe to the seams between the stator, the back iron and the supporting structure. Because of the low viscosity, some epoxy wicks in between the layers. This small amount of wicking increases the strength of the attachment. Copper windings are laid on one by one, and more epoxy is used to fill the gap between stator poles and the copper winding. After the application of epoxy, the whole assembly is sandwiched between precisely machined flat steel plates and weighed down with other heavy steel plates. The stator assemblies are left to dry for several days. Figure 4-10a shows one of the resulting stator assemblies.

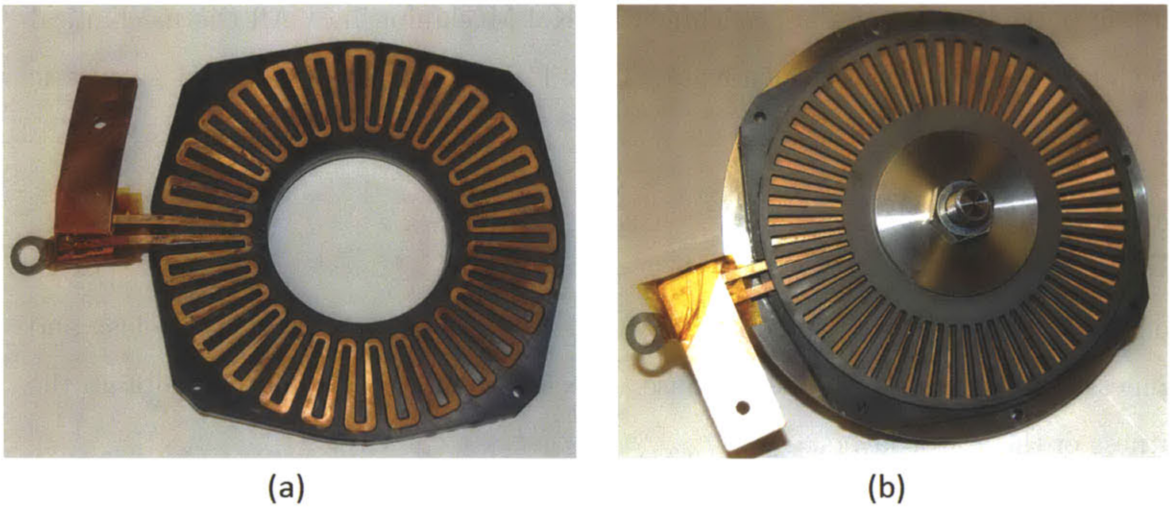
(a) (b)

Figure 4-10: Assembled (a) stator piece (b) stator & rotor piece.

The bearing set and the axle are then mounted to the stator and its supporting structure. The bearing set is first slid into the housing by hand. Then the bearing inner ring is supported on an arbor press and the axle is pressed into the ring. It is important that no force is applied to the bearing balls or to the outer ring during the press fit. The rotor stiffener plates and the rotor are then bolted to the axle. Figure 4-10b shows the resulting stator and rotor assembly. Finally, the two stators are bolted together with machine screws around the perimeter and kept apart with precision gauge blocks.

4.4 Summary

This chapter presented the mechanical design process, including the bearing housing geometry calculations and rotor stiffness analysis. It also detailed the motor fabrication and assembly procedure. In particular, the ferrite plates experiences cracking problems during water jetting, which is solved by adding aluminum sheets as back support. During assembly, the stator is attached to the supporting structure with thinned epoxy. The epoxy is only applied to the seams to maintain stator alignment.

Chapter 5

Experiments and Results

This chapter presents the experiments performed and the data collected. The experimental data is compared with the model predictions, aiming to prove the correctness of the models. The physical geometric characteristics of the stator, rotor and axle planes are discussed, including their flatness, parallelism and stiffness. Furthermore, the flux linkage and the torque measurements are described. The dimensions of the prototype measured is listed in the Column 1 of Table 3.3.

5.1 Mechanical Measurements

Once the one-phase SVRM prototype is assembled, many of its geometric characteristics are measured with a CMM. The measurements focus on determining whether the 50 μm can be maintained between the stator and rotor plates. The results are compared to the mechanical design to verify the calculations. The measured surfaces, as shown in Figure 5-1, are the rotor plane, the stator plane and the axle plane. The bearing housing plane is used as the reference plane for all the measurements.

5.1.1 Parallelism

The rotor is first removed and the left stator surface is measured for its flatness and parallelism. The left stator has two separate concentric parts made from a single piece

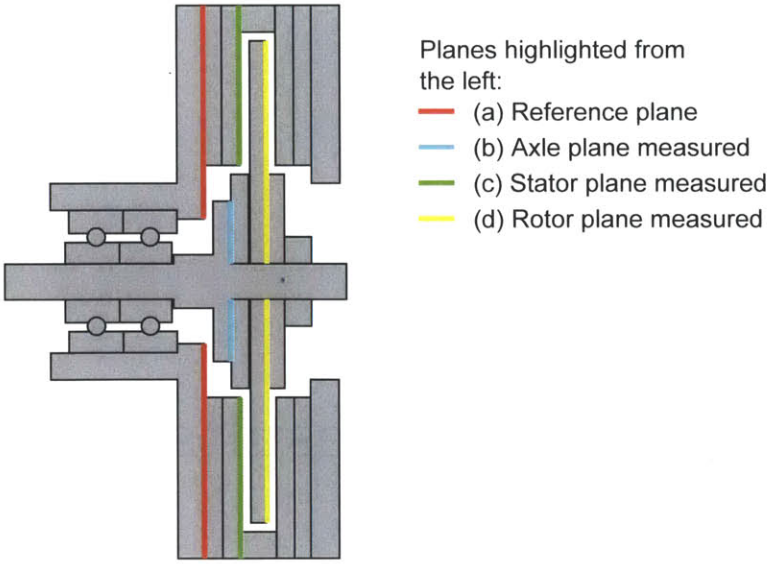

Figure 5-1: Surfaces measured. (a)The housing plane was used as the reference plane for all other measurements. The results of (b), (c) and (d) are shown in Figure 5-3, Figure 5-2, Figure 5-4.

of ferrite. The errors in the flatness of both pieces are nearly the same, at around $\pm 10\ \mu m$. In addition, their flatness is the same as the stock material, meaning there is minimal internal stress in 3C97 stock and that the water jet cutting did not distort the material.

The stator pieces are adhered to the back iron plate, which is adhered to the bearing housing using epoxy. The epoxy application techniques described in Subsection 4.3.3 aim to keep the stator, the back iron and the bearing housing parallel to each other, as well as to keep the gaps between them small. The error in the parallelism between the stator and the bearing housing, shown in Figure 5-2, is about $\pm 15\ \mu m$ (Outliers are disregarded.). This result is quite good, given that the original error in the parallelism of the stator and rotor stock material is about $\pm 10\ \mu m$.

The second measured surface is the axle plane, as illustrated in Figure 5-1b. The measurements are made to verify the bearing misalignment angle and the rotor tip axial displacement calculation discussed in Subsection 4.2.1. The error in the flatness of the rotor surface is measured to be $\pm 2\ \mu m$. The error in the parallelism of the axle plane is measured at four different rotor angles (0°, 90°, 180° and 270°). The result at

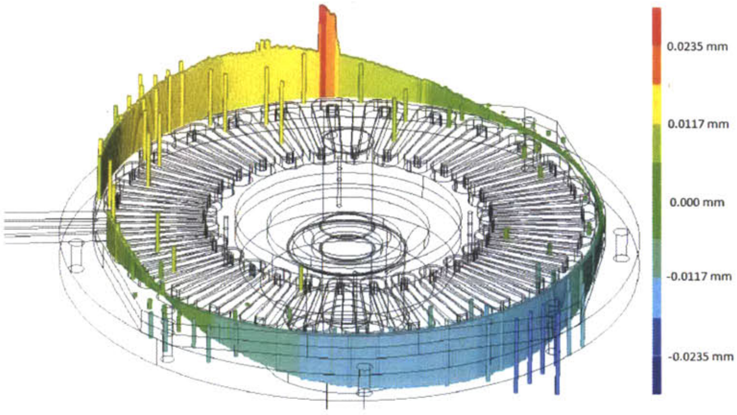

Figure 5-2: Errors in the parallelism of the stator surface.

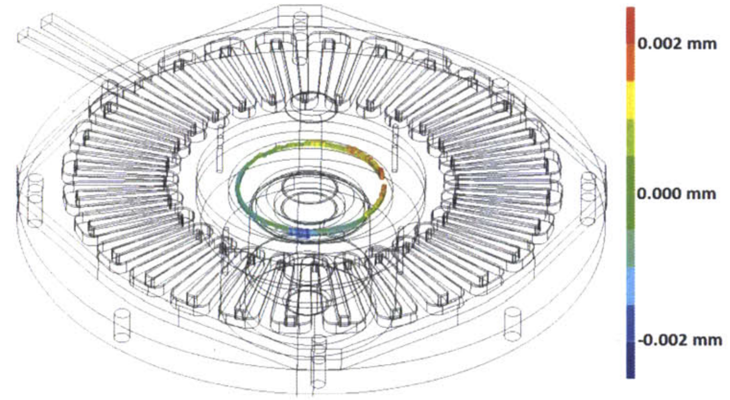

Figure 5-3: Errors in the parallelism of the axle surface.

0° is shown in Figure 5-3. The largest axial travel at the tip of the axle plane is ±3.5 μm, meaning the axle misalignment angle is well within the designed worst case.

The rotor plate is sandwiched between two rotor stiffener plates. All three plates are slid down the axle and pushed tightly against the axle plane by the axle nut. The nut must exert enough axial force on these three plates so that the static friction between them is large enough to prevent the rotor from slipping when the motor is excited. However, this force from the nut has a substantial influence on the parallelism of the rotor plate. Figure 5-4 compares the errors in the parallelism of the rotor with and without the nut. When the nut is tightened, the axial displacement of the rotor

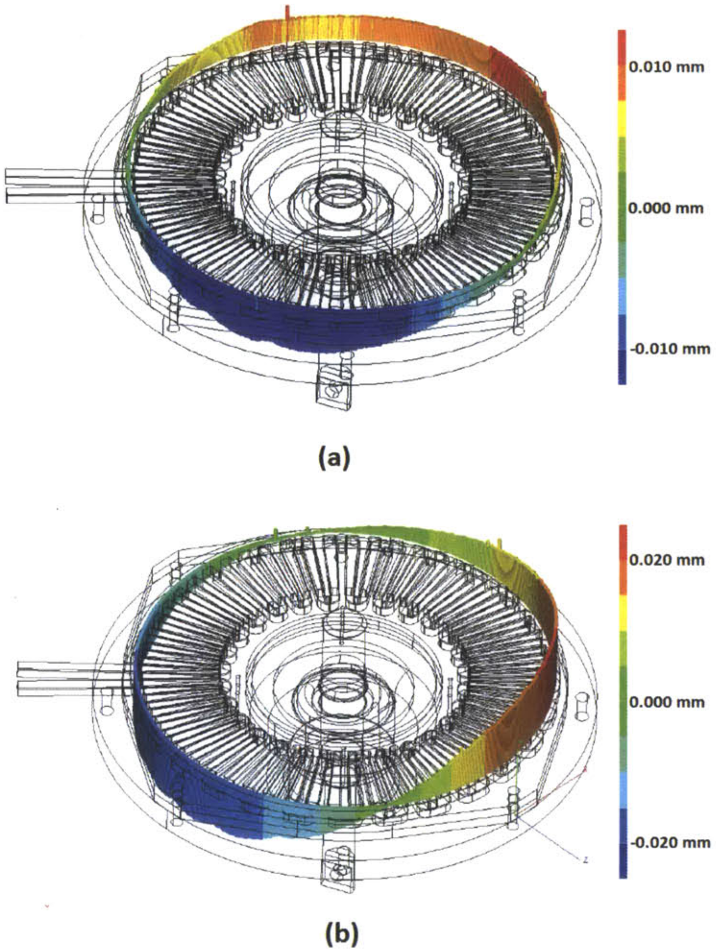

Figure 5-4: Measured error in the parallelism of the rotor (a)without and (b)with the axle nut.

tip doubles from ±10 μm to ±20 μm. This misalignment is caused by the uneven force that the nut exerted on the rotor stiffeners and the rotor plate. The nut used is not precision machined and the side surfaces of the nut are not ground. The thread axis is then not exactly perpendicular to the two side surfaces of the nut. Therefore, when the nut is tightened, one corner of the nut exerts more force and causes the rotor to tilt to one side.

One solution to this nut problem is to precision machine a nut and grind the surfaces of the nut to make sure the force from the nut on the rotor plate is evenly distributed around the axle. In addition, class 3 threads should be used on the axle and the nut to reduce the nut wobble. This solution, however, requires a new axle and a new nut, which are relatively difficult to machine. Another solution to the nut problem is to increase the air gaps slightly by using a thicker rotor stiffener and thicker gauge blocks. When the gap is larger, the nut can be tightened without causing rotor tip to touch the stator surface. The latter solution is ultimately chosen because of its simplicity. The air gaps of the motor are increased from $50\mu m$ to $100\mu m$ for static torque measurements.

5.1.2 Bearing Stiffness

When the motor poles are excited, there is an axial force on the rotor because the rotor is not perfectly centered. With a proper preload, the bearing set should be stiff enough to prevent the axle from moving too much axially and thus prevent the air gaps from collapsing. This criteria is verified by bearing stiffness measurements. Different weights are put on axle and the axial travels of the axle are measured using a CMM, shown in Figure 5-5. A linear regression estimates the stiffness of the bearing set at 5.631 $N/\mu m$, which is stiff enough for this application.

5.1.3 Mechanical Conclusions

The above measurements have shown that the mechanical design and the assembly techniques are successful at keeping the stator and rotor plates parallel enough very small air gaps. This is verified by the fact that with two $50\mu m$ air gaps and the axle nut loosely attached, the rotor can be spun freely by hand without scraping the stator surfaces. The motor, however, fails at maintaining the $50\mu m$ air gaps when the axle nut is tightened. Unfortunately, a loosely attached nut cannot prevent the rotor from tilting when the windings are excited. The uneven axial magnetic force pushes one side of the loose rotor to the adjacent stator plate. In addition, a loose nut does not provide enough normal force and thus not enough static friction to prevent the rotor from slipping when the rotor is under load. Ultimately, a larger 100 μm air gap is used to allow the nut to be completely tightened for static torque measurements.

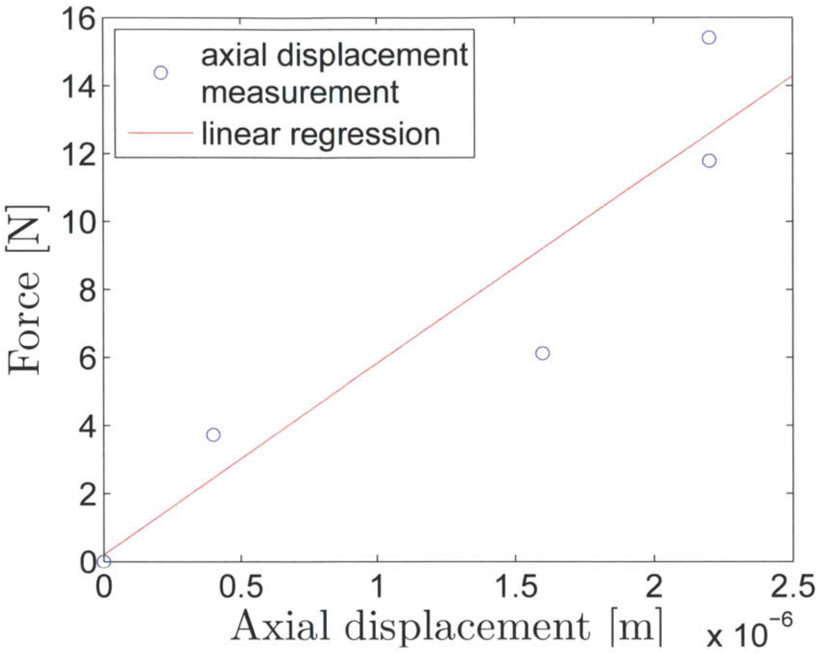

Figure 5-5: Bearing stiffness measurements and the linear fitting.

However, it is believed that a 50 μm air gap is achievable with a precision ground axle nut and tighter threads.

5.2 Magnetic Flux Linkage Measurements

5.2.1 Experimental Setup

One of the most important goals of the model is to correctly predict the relationship between the current in the cooper winding and the flux linked by the winding, as described in Chapter 3. In order to verify such curves experimentally, a large current must be injected into the motor coil and the flux linkage or an equivalent information must be measured simultaneously. The method used to inject large current in this thesis is to discharge a capacitor bank directly to the motor coil. The schematic of the circuit used is shown in the Figure 5-6.

The circuit has two parts. The left side of the circuit contains a power supply, a charging power resistor and a switch. These components form the capacitor bank

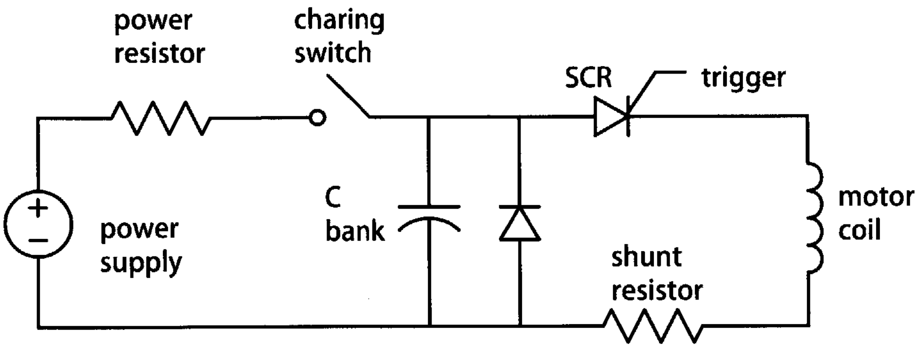

Figure 5-6: Circuit schematic for flux linkage experiments. Component values are listed in Table 5.2.

charging circuit. On the right side of the schematic, a silicon-controlled rectifier (SCR), an inductor (used to model the motor coil), a shunt resistor and a free wheeling diode form the discharging circuit. An SCR, or thyristor, is a solid state switch that can be turned on by a low voltage triggering signal. It can carry large currents with minimal resistance in one direction and withstand large voltages in the opposite direction. It is the ideal switch for the discharge circuit. The shunt resistor is a resistor with a small, precise and stable resistance, which can be used to measure current in the loop using Ohm's Law.

In the beginning of the experiment, the charging switch is closed and the SCR is open. The capacitor is charged to the supply voltage through the charging power resistor which is chosen to limit inrush current. The supply voltage required to inject a certain peak current into the windings depends on the maximum storage capacity of the motor coil and the total series resistance in the discharge circuit loop. The supply voltage was experimentally determined. When the capacitor bank is getting charged, the charging power resistor restricts the charging current, and thus protects the capacitor bank and the power supply from the extreme inrush current.

Once the capacitor bank is charged to the appropriate voltage, the charging switch is opened and the discharing circuit can be simplified to a RLC circuit shown in Figure 5-7. The motor coil is modeled by an ideal inductor L_m in series with a linear resistor R_m. The resistance of the shunt resistor, the on-state resistance of the SCR and all other parasitic resistances are lumped into one R_p. When the trigger is pulled

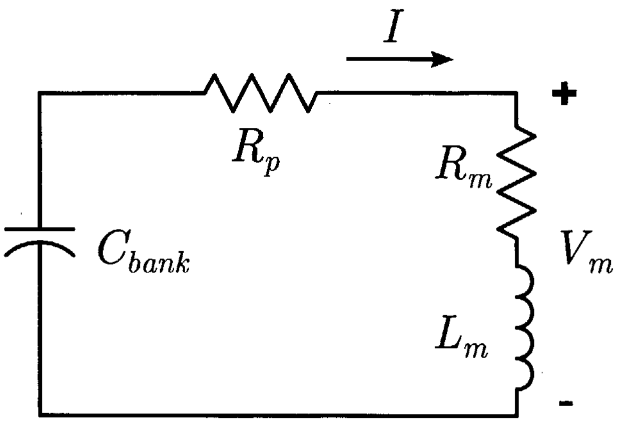

Figure 5-7: RLC equivalent of the discharging circuit.

high by a low voltage signal, current flows out of the capacitor bank and into the inductor at a very high rate. The voltage V_m across the motor coil is

$$V_m(t) = V_R + V_L = I(t)R_m + \frac{d\lambda(t)}{dt} \tag{5.1}$$

where $I(t)$ can be calculated from the voltage $V_s(t)$ across the precision shunt resistor. Rearranging the terms of (5.1) yields,

$$\frac{d\lambda(t)}{dt} = V_m(t) - I(t)R_m \tag{5.2}$$

The flux linkage can then be calculated by integrating (5.2) according to

$$\lambda(t) = \int_0^t (V_m(t') - I(t')R_m)dt' \tag{5.3}$$

Thus, both the flux linkage and the current can be determined with respect to time. They can be plotted against each other as in Figure 3-15.

As the rotor does not experience torque at the both the aligned position and the unaligned position, rotor slipping does not occur at these two position. The axle did not need to be completely tightened for the flux linkage measurements. Some small axial motion may exist during the experiment, but the axial motion has negligible effect on the flux linkage. Therefore, the maximum and minimum flux linkage curves could be measured with 50 μm, 75 μm and 100 μm air gaps. Table 5.1 lists the components used for the flux linkage measurements. An impedance analyzer is used to measure relevant component values for the experiment. Results are shown in Table 5.2.

Component	**Manufacturer & Name**	**Relevant Spec**
Capacitor bank	Vishay	33 mF (8 in parallel)
SCR	Powerex T720	
Capacitor protection diode	Vishay 45L(R)	
Shunt resistor		0.01 Ω resistance
Scope	Tektronix TDS 3034B	4 channel with data logging
Impedance analyzer	HP 4192A	

Table 5.1: List of components used in the magnetic flux linkage measurement setup

Parameter	**Value Measured**	**Unit**
C_{bank}	0.24	F
R_{bank}	0.5	mΩ
R_{shunt}	0.01	Ω
R_{motor} (room temp)	0.268	Ω

Table 5.2: Measured component values

5.2.2 Theory Comparison and Material Property Adjustment

The flux linkage versus current measurements are compared to the same relation predicted by the total model in Section 3.3. The measured flux linkage curves and the model predictions are plotted in Figure 5-8 for a 75 μm air gap.

The experimental minimum flux linkage curve appears to be drastically different from the model prediction. The experimental minimum flux linkage curve reveals a lot about the prototype machine. The minimum flux linkage curve has three distinctive regions, as labeled in Figure 5-8. Region 1 has much higher slope than the model prediction, meaning there is a flux path in the prototype that had not been considered in the total model. This extra path comes from the outer and inner rims of the rotor and stator, shown in Figure 4-8. The rims are included to give structural support to

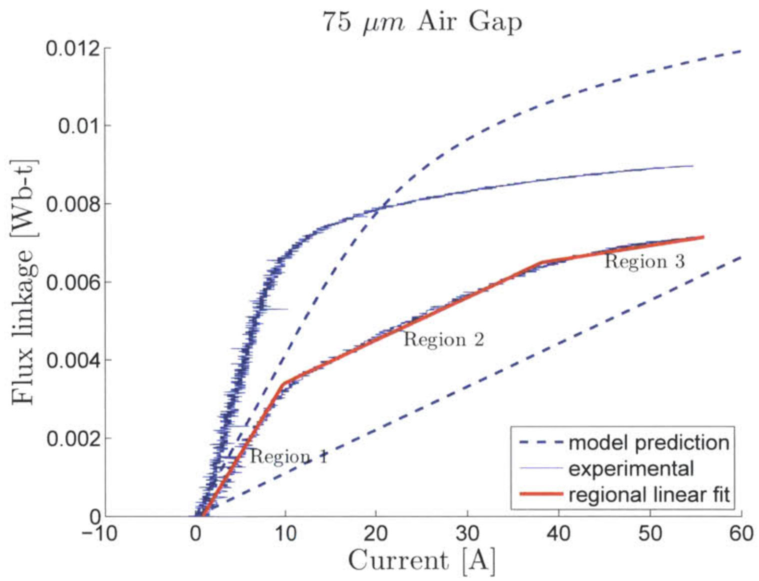

Figure 5-8: Initial comparison of maximum (aligned position) and minimum (unaligned position) flux linkage curves at 75μm.

the stator and rotor poles. Without the rotor outer rim, each rotor pole is a cantilever beam which would be structurally weak. The addition of the rims effectively increases the length of the stator and rotor poles in the aligned position and provides an extra low reluctance path for the flux in the unaligned case. In both aligned and unaligned positions, the inductance in Region 1 is increased by the **rim effect**, though by slightly different amount.

Region 2 is the linear region of the minimum flux linkage curve. As the current increases above Region 1, the thin rotor outer rim saturates and the flux is forced to flow across the large air gaps as expected in the unaligned position model. Therefore, the magnetic reluctance experienced by the flux is the same as the model and the measured incremental change in flux linkage is the same as what the model predicts. This is shown by the fact that the slope of the model prediction and the slope of the experimental curve are the same in Region 2.

Region 3 is the saturation region of the unaligned case. This effect does not show up on the model prediction. The absence of saturation reveals that the material permeability curve used by the model was incorrect.

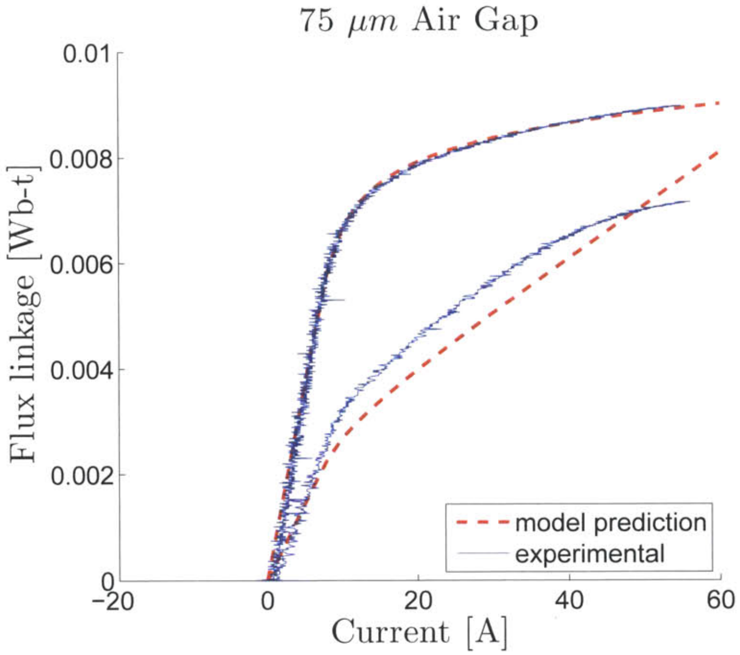

Figure 5-9: Comparison of maximum and minimum flux linkage curves at 75μm with modified permeability model.

The problems revealed by the minimum flux linkage curve also cause the model predicted maximum flux linkage curve to differ from the measured curve. The rim effect causes the measured maximum flux linkage curve to have higher initial slope. Additionally, the incorrect permeability curve causes the model curve to saturate much later.

The remainder of this section aims to include these two changes in the model. The rim effect is relatively easy to incorporate in the maximum flux linkage curve, because the rim effect essentially increases the length of the magnetic poles in the aligned position. Therefore, the pole length used in the model is increased until the initial slope matched the experimental curve.

For the material saturation effect, even though model prediction does not match the experimental result, the shapes of the maximum flux linkage curves are similar. This similarity in the maximum flux linkage curves means that the type of functions used in Subsection 3.2.1 to model the $\mu(H)$ was correct, but the constants used were wrong. Thus, different constants are tried until the model predicted maximum

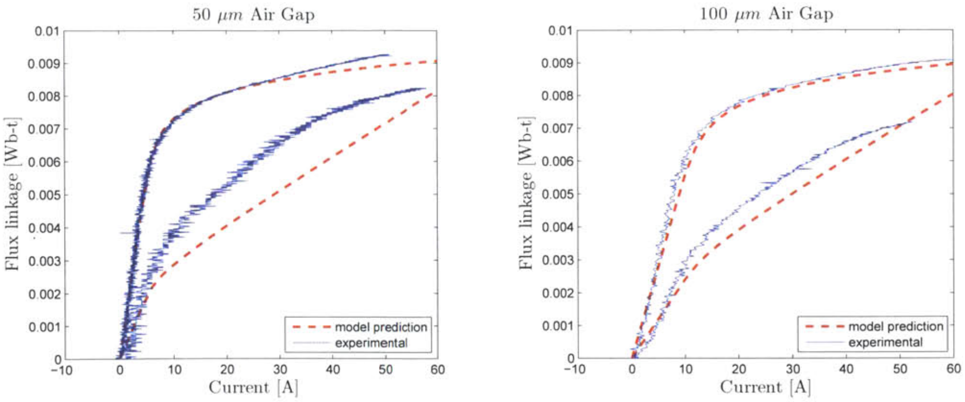

Figure 5-10: Comparison of maximum and minimum flux linkage curves at $50\mu m$ and $100\mu m$ air gaps, with modified permeability curve and the rim effect.

flux linkage saturation matches the experimental values at 75 μm air gaps, shown in Figure 5-9. The resulting $\mu(H)$ for the ferrite used is

$$\mu(H) = 0.2051(\frac{H}{H_0})^{-0.92}(H/m) \tag{5.4}$$

where $H_0 = 1\ A/m$.

The same pole length increase and the modified permeability curve (5.4) are also applied to 50 μm and 100 μm air gap models. The modified maximum flux linkage models match very well with the experimental ones for these two new gap sizes, shown in Figure 5-10. This validates the correctness of the modifications.

The same permeability curve can be easily applied to the minimum flux linkage (unaligned position) model. However, the rim effect cannot be as easily applied to the minimum inductance model, because the rim flux changes the symmetry of the 3D unit cell discussed in Section 3.1, and it can no longer be simplified into a 2D model. However, it is found that the rim effect increases both the maximum and minimum flux linkages by a similar amount. Therefore, the minimum flux linkage with the rim effect can be roughly estimated using the 2D model and the rim effect difference from the maximum flux linkage curves, expressed by

$$\lambda_{min\ w/\ rim}(i) = \lambda_{min\ w/o\ rim}(i) + [\lambda_{min\ w/\ rim}(i) - \lambda_{min\ w/o\ rim}(i)]. \tag{5.5}$$

Component	Manufacturer & Name	Relevant Spec
Load cell	Omega LCR-25	S-beam load cell at 25lb max
Load cell signal amp	Omega DMD-465WB	
Shunt resistor		0.01 Ω resistance
Scope	Tektronix TDS 3034B	4 channel with data logging
Power supply	HP 6011A	1000W 120A
Laser pointer		generic

Table 5.3: List of components used in the static torque measurement setup

The resulting minimum flux linkage estimation curves are also shown in Figure 5-9 and Figure 5-10. It can be seen from the graphs that the estimation curves are below the experimental curves, meaning that the unaligned position rim effect is larger than the aligned position rim effect. The rim effect reduces the area enclosed by the two flux linkage curves. Therefore, if the rims can be removed, the torque produced by the machine can increase.

5.3 Static Torque Measurements

5.3.1 Experimental Setup

The static torque measurements aim to find the relations between the torque and the angle of the rotor, as well as the torque and the current. The static torque is measured using an aluminum lever arm connected with a load cell. The load cell is a strain gauge-based force sensor. The signal from the load cell is amplified and fed into an oscilloscope. A laser pointer, mounted on the lever arm, projects a light dot on the wall across the room. The angle of the lever arm is calculated from the location of the dot on the wall. Current in the winding is measured with a 0.01 Ω shunt resistor. The setup is shown in Figure 5-11 and the relevant components are listed in Table 5.3. All torque measurements are done with 100 μm air gaps.

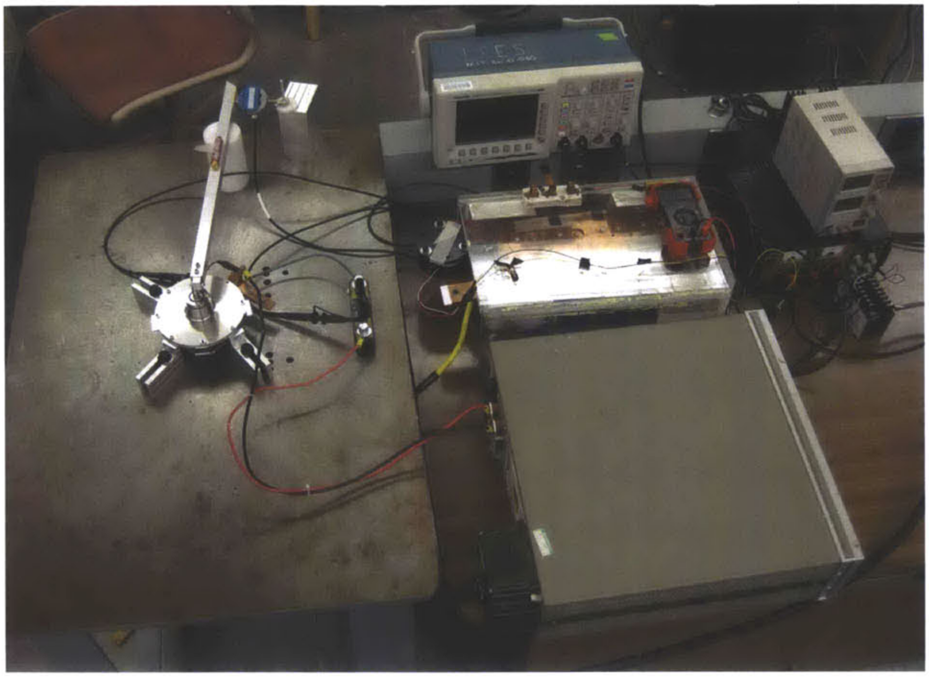

Figure 5-11: Experimental setup for measuring static torque of the motor.

5.3.2 Comparison with Theory

There are three different ways to determine the torque output of the motor. Firstly, the average motor torque can be predicted by the energy conservation method and the total model presented in Chapter 3. The torque can also be directly calculated from the unit cell using FEA. Lastly, the torque can be experimentally measured. This subsection compares the results of all three methods.

The energy conservation method computes the average torque produced by the motor over an electrical cycle at a constant current or zero, but it does not produce the torque versus angle relationship. The FEA, however, can be used to calculate torque at any given angle. Figure 5-12 shows the magnetic flux pattern in a unit cell at a typical misaligned position, calculated using FEA. The setup of the FEA for the misaligned position is very similar to both the aligned and the unaligned position FEA presented in Section 3.3. Forces on the rotors can be integrated in the FEA software. The torque produced is then easily found using $\tau = \mathbf{r} \times \mathbf{F}$. The energy conservation method and the FEA force calculation produce the essentially

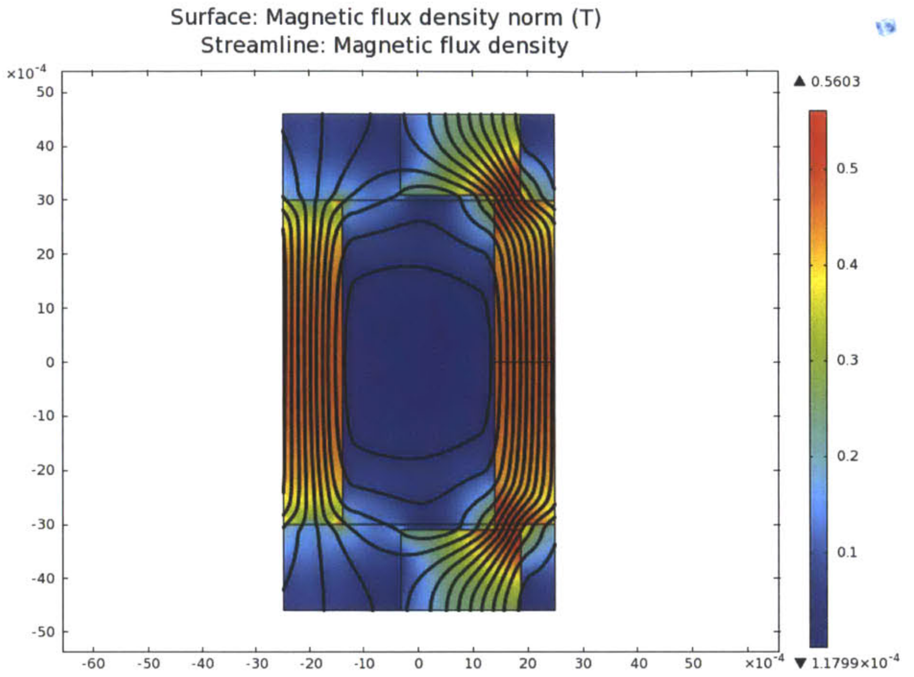
Surface: Magnetic flux density norm (T)
Streamline: Magnetic flux density
×10⁻⁴
50
40
30
20
10
0
-10
-20
-30
-40
-50
-60
-50
-40
-30
-20
-10
0
10
20
30
40
50
×10⁻⁴
▲ 0.5603
0.5
0.4
0.3
0.2
0.1
▼ 1.1799×10⁻⁴

Figure 5-12: The flux pattern for a misaligned position. The force on the rotor poles can be directly calculated from the magnetic fields.

the same average torque over an electrical cycle. The torque calculated by the pure FEA method is 4.5% lower than the energy conservation method at the rated 80A current and 100 μm air gaps. The difference can be contributed to the coarse grid used by the FEA method (32 points over the entire electrical period).

The motor torque is measured over half an electrical cycle with a 30A winding current. The air gaps are set at 100μm. The results are plotted against the FEA prediction with modified permeability curve in Figure 5-13. Even though the FEA force calculation does not take the rim effect into consideration, the FEA torque prediction and the measured torque match pretty well. This may seem peculiar initially. However, it can be explained by the energy method. Figure 5-14 compares the flux linkage curves predicted by the model and the measured flux linkage curves. It is clear that the model does not predict the flux linkage well when the rim effect is not taken into consideration. However, the rim effect at 100 μm air gaps raises both the maximum and minimum inductances by a similar amount, and thus the area enclosed by the theoretical curves and the area enclosed by the experimental

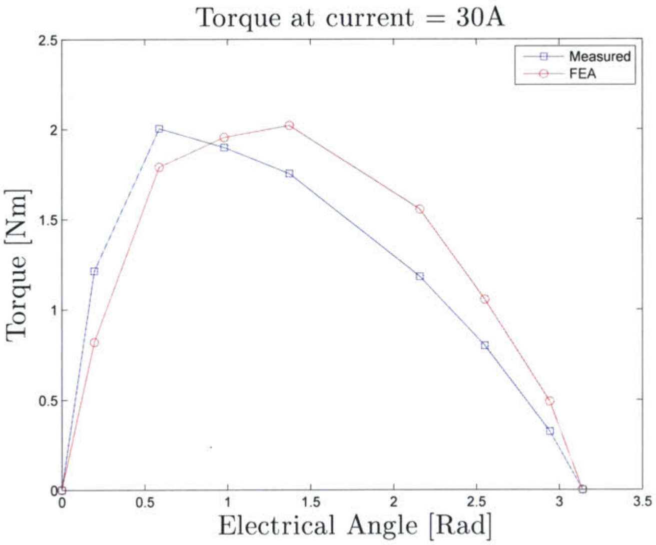

Figure 5-13: Torque produced at 30A over half of an electrical cycle with 100 μm air gaps.

flux linkage curves are very similar between 0A and 30A. This is also verified by the fact that the unaligned flux linkage estimation curve in Figure 5-10b is close the experimental one. Therefore, the average torque predicted by the energy conservation model matches the actual torque produced, as does the FEA torque prediction.

Later, the rotor is also fixed at two random misaligned position with electrical angles of 0.589 *Rad* and 0.982 *Rad*. Current is driven into motor to the limit of the power supply. The measured torque is plotted against the FEA prediction over a large range of currents. The FEA results are similar in shape to the experimental value, especially at low current. The difference between the two at higher currents is believed to be due to the rim effect.

5.4 Optimization with Modified Permeability Curve

Because the permeability curve for ferrite is modified according to the experimental data, the optimal design is no longer the same. Another round of the optimization process is carried out without practical constraints for motors with no more than 100 pole pairs and with 100 μm air gaps. The resulting optimal is listed in Table 5.4.

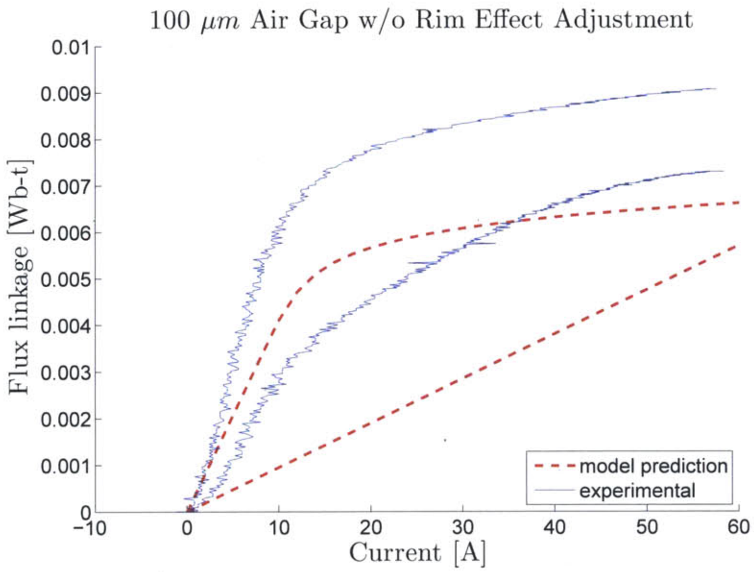

Figure 5-14: Flux linkage versus current plot with modified permeability curve, but without rim effect adjustment.

Material	3C97
Outer radius [mm]	57.9
Inner radius [mm]	45.9
Number of pole pairs	100
Stator width / rotor width	0.71
Stator thickness [mm]	0.96
Rotor thickness [mm]	1.18
Number of rotors per phase	1
Performance	
Maximum current [A]	297
Torque [Nm]	1.55
Torque/weight [Nm/kg]	**8.41**
Torque/volume [Nm/m^3]	0.4×10^4

Table 5.4: Optimal designs with modified ferrite permeability for motor with 100 μm air gaps.

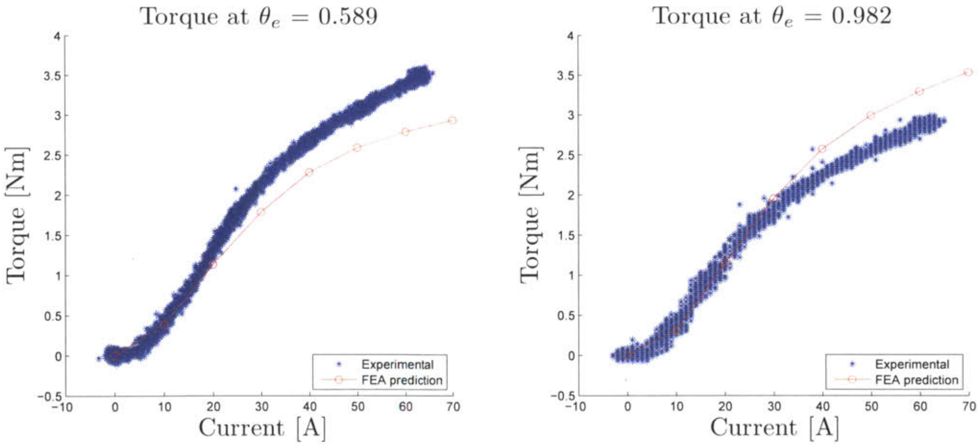

Figure 5-15: Torque versus current at two different electrical angles.

5.5 Summary

The mechanical measurements verifies that the design and assembly of the mechanical parts in the motor is successful at maintaining small air gaps. It also shows that the axle nut introduced a non-negligible imbalanced axial force that causes the rotor to tilt. As a consequence, all torque measurements are done with 100 μm air gaps.

The magnetic flux measurements reveals that the rims of the rotor have a large effect on the flux linkage and the permeability curve used was incorrect. With permeability and rim effect corrections, the maximum flux linkage curves predicted by the model match the experimental curves very well. The minimum flux linkage estimation curves match the experimental curves with some limited success.

The torque measurements show that the energy conversation method, the pure FEA method both match well with the experiments. The peak measured torque at 30A is 2 Nm for the one phase prototype with 100 μm air gaps. With the same motor dimensions, the models predict that a peak torque of 4.29 Nm and an average torque of 1.6 Nm can be achieved at peak current of 80A with 50 μm air gaps.

The active mass of the single-phase motor is 0.5 kg and the combined mass of all structural parts, including the bearing housing, the bearings, the axle and other parts, is 1.7kg. The structural parts reduced the torque-to-mass ratio of the one phase prototype substantially. However, a three-phase motor with the same dimensions can triple the output torque of the motor while keep the structural mass almost constant.

Chapter 6

Conclusions

The thesis set out to explore a new type of motor, the SVRM, which has a lot of advantages over existing motors. The objectives of the thesis are to:

- develop a flexible model that predicts the SVRM performance accurately and efficiently over a large geometric design space;
- optimize the design of a motor for high torque-to-mass ratio with a given maximum heat dissipation rate and a maximum dimension;
- experimentally verify the model accuracy, and to correct any errors in the model using the collected experimental data.

6.1 Summary

This thesis first developed a hybrid model that contains an analytical maximum flux linkage model and a numerical minimum flux linkage model. The hybrid model has an advantage over a pure analytical model due to its versatility and correctness, and over a pure numerical model due to its speed. An energy conservation method is used to calculate the average torque of the motor over an electrical cycle based on the hybrid model.

An optimization process is performed for designing a hip motor for the MIT cheetah robot. Both steel and ferrite are considered for constructing the motor, and the permeability curves of both materials are extrapolated for optimization purposes. With 50 μm air gaps, the initial optimization puts the theoretical maximum torque-to-mass ratio of the steel motor at 35.7 Nm/kg and the theoretical maximum torque-to-mass ratio for a ferrite motor at 22.2 Nm/kg. However, concentric or wedge-shaped steel laminations are not available, and the severe skin effect of solid steel core renders the steel design useless at speed. Thus, the steel design is not implemented. Furthermore, some other practical constraints reduce the torque-to-ass ratio of the ferrite motor down to 9.4 Nm/kg.

A single-phase prototype is constructed based on the optimization results. The prototype has two adjustable air gaps. Flux linkage curves are measured at the aligned and unaligned positions with 50 μm, 75 μm and 100 μm air gaps. The ferrite permeability model is found to be incorrect, and the rotor structural rim has a substantial influence on the flux linkage. The model matches with the experimental values very well after these two corrections. Unfortunately, with the modified permeability curve of ferrite, the model showes that the torque-to-mass ratio of the prototype is further reduced to only $3.1 Nm/kg$.

6.2 Conclusions

A single-phase SVRM prototype is constructed using ferrite 3C97. The ferrite has proven to be structurally tough enough to produce decent torque without breaking and stiff enough to maintain 100 μm gaps. It is believed that 50 μm air gaps are also feasible with a ground axle nut and tighter threads. There is a 15% torque increase when reducing the air gaps from 100 μm to 50 μm at the dimensions of the prototype.

The peak measured torque at 30A is 2 Nm for the one-phase prototype with 100 μm air gaps. The models predict that a peak torque of 4.29 Nm and an average torque of 1.6 Nm can be achieved at peak current of 80A with 50 μm air gaps.

The active mass of the single-phase motor is 0.5 kg and the combined mass of all structural parts, including the bearing housing, the bearings, the axle and other parts, is 1.7kg. The structural parts reduce the torque-to-mass ratio of the one phase prototype substantially. However, a three-phase motor with the same dimensions can triple the output torque of the motor while keeping the structural mass almost constant. Furthermore, if more rotor and stator plates are included per phase, the additional structural mass is still minimal, meaning if enough stator and rotors are used the torque-to-total-mass ratio of the entire motor approaches to the torque-to-active-mass ratio of the motor.

The model developed in this thesis is very successful at predicting the flux linkage curves and output torque of the prototype, after material property corrections. Another round of the optimization process is carried out for ferrite motors with no more than 100 pole pairs and with 100 μm air gaps, and the best torque-to-mass ratio found is 8.4 Nm/kg. It is concluded that ferrite's flux carrying capacity is insufficient for high toque-to-mass ratio motors, given the requirements of the hip motor.

The copper conduction loss is capped at 2400W at operating temperature according to the design requirement for the cheetah hip motor. The winding packing factor in the model is assumed to be 100%, which is higher than the prototype, so the copper resistance of the prototype is a bit higher. However, the total resistance of the copper winding is 0.268 Ω, meaning total conduction loss of 2572 Watts at room temperature, still reasonably close to the model.

6.3 Future Work

The rim effect introduces a lot of complexity into the magnetic model. A non-magnetic rim could made to replace the ferrite rim. In this case, it would not only reduce the modeling complexity, but also potentially increase the torque produced.

No controller has been designed or constructed for the prototype motor. The dynamics of a SVRM have not been explored and experimented. One potential challenge of the SVRM control comes from the large number of pole pairs, causing a very high electrical frequency when motoring. It is difficult to predict what effect the high electrical frequency will have on the performance of the motor.

Due to the lack of commercially available concentric or wedge-shaped steel laminations at the time of this writing, the steel design is not constructed. However, the steel motor has much higher torque-to-mass ratio than the ferrite counterpart. Custom lamination could be explored.

Other case studies should be experimented with SVRM. The author believes there are better motor dimensions that show the performance advantages of SVRMs. The hip motor was too narrow and thus only one rotor is used per phase. Other design metrics such as torque density could also be explored.

Appendix A

Mechanical Drawings

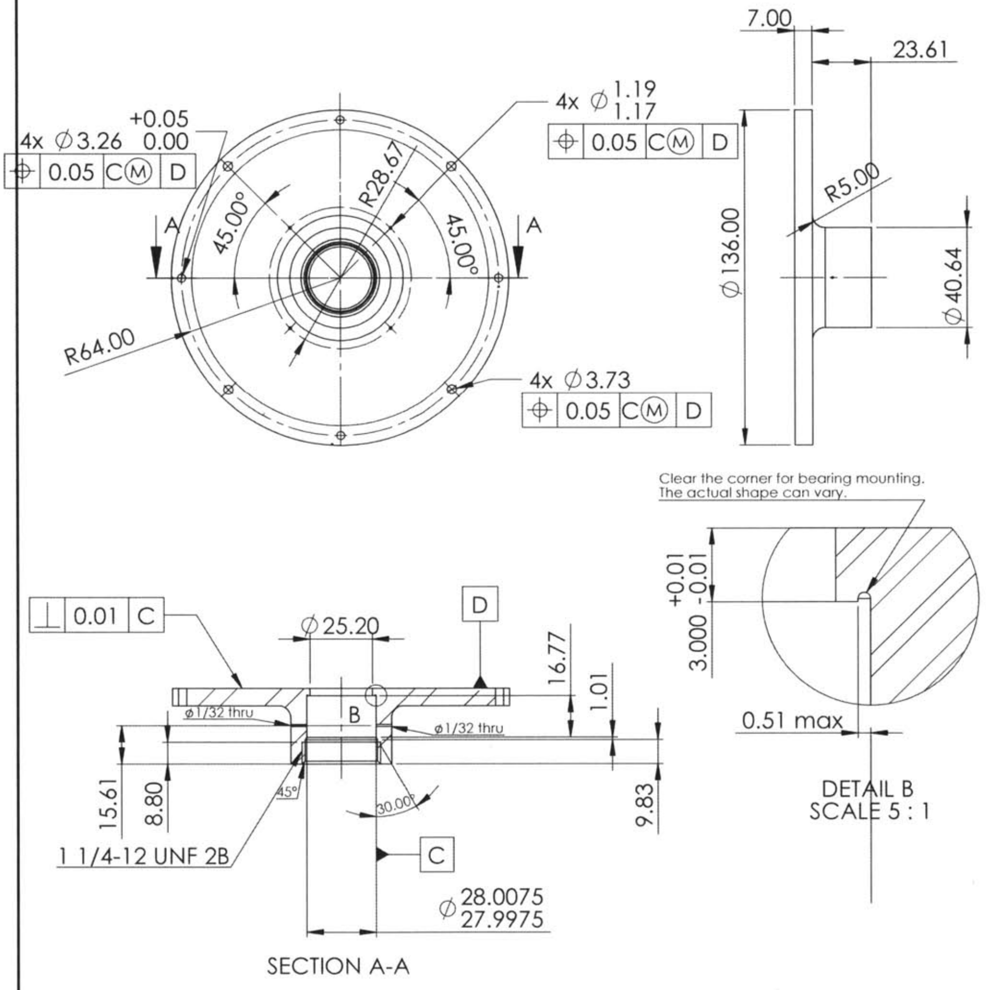
7.00
23.61
4x ∅ 1.19 1.17
⌖ 0.05 C Ⓜ D
+0.05
4x ∅3.26 0.00
⌖ 0.05 C Ⓜ D
R28.67
45.00°
45.00°
A
A
R5.00
∅136.00
∅40.64
R64.00
4x ∅3.73
⌖ 0.05 C Ⓜ D
Clear the corner for bearing mounting.
The actual shape can vary.
+0.01
3.000 -0.01
⊥ 0.01 C
D
∅25.20
16.77
1.01
ø1/32 thru
B
ø1/32 thru
15.61
8.80
45°
30.00°
9.83
0.51 max
DETAIL B
SCALE 5 : 1
1 1/4-12 UNF 2B
C
∅ 28.0075 27.9975
SECTION A-A

UNLESS OTHERWISE SPECIFIED:
DIMENSIONS ARE IN MILLIMETERS
TOLERANCE:
WHOLE NUMBER DIM'S: ±1
ONE PLACE DECIMALS: ±0.5
TWO PLACE DECIMALS: ±0.05
ANGLES: ±0.5 DEG

FINISH:

DEBUR AND BREAK SHARP EDGES

DO NOT SCALE DRAWING

REVISION 1.0

	NAME	SIGNATURE	DATE
DRAWN			
CHK'D			
APPV'D			
MFG			
Q.A			

TITLE:

MATERIAL:
S STEEL

WEIGHT:

DWG NO.
mountingend

A4

SCALE:1:2

SHEET 1 OF 1

SolidWorks Student License
Academic Use Only

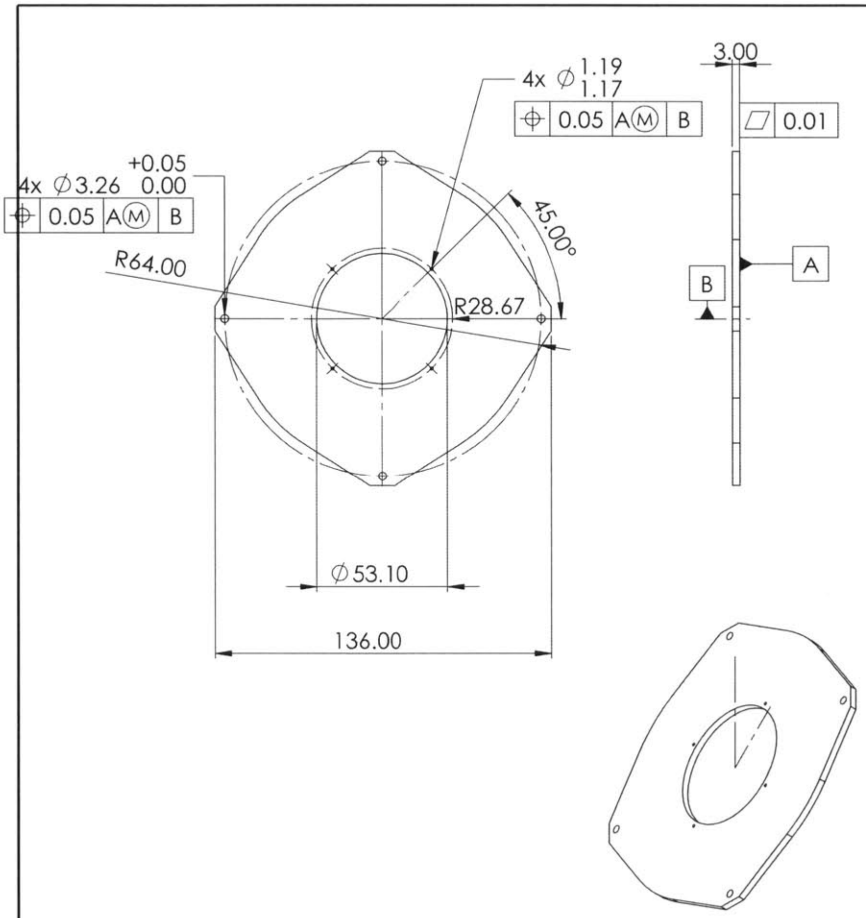

3.00
4x ⌀ 1.19 1.17
⌖ 0.05 Ⓜ A B
▱ 0.01
+0.05
4x ⌀3.26 0.00
⌖ 0.05 Ⓜ A B
45.00°
R64.00
R28.67
A
B
⌀53.10
136.00

UNLESS OTHERWISE SPECIFIED:
DIMENSIONS ARE IN MILLIMETERS
TOLERANCE:
WHOLE NUMBER DIM'S: ±1
ONE PLACE DECIMALS: ±0.5
TWO PLACE DECIMALS: ±0.05
ANGLES: ±0.5 DEG

FINISH:

DEBUR AND BREAK SHARP EDGES

DO NOT SCALE DRAWING

REVISION 1.0

	NAME	SIGNATURE	DATE
DRAWN			
CHK'D			
APPV'D			
MFG			
Q.A			

TITLE:

MATERIAL:
S STEEL

DWG NO.
mountingend2

A4

WEIGHT:

SCALE:1:2

SHEET 1 OF 1

SolidWorks Student License
Academic Use Only

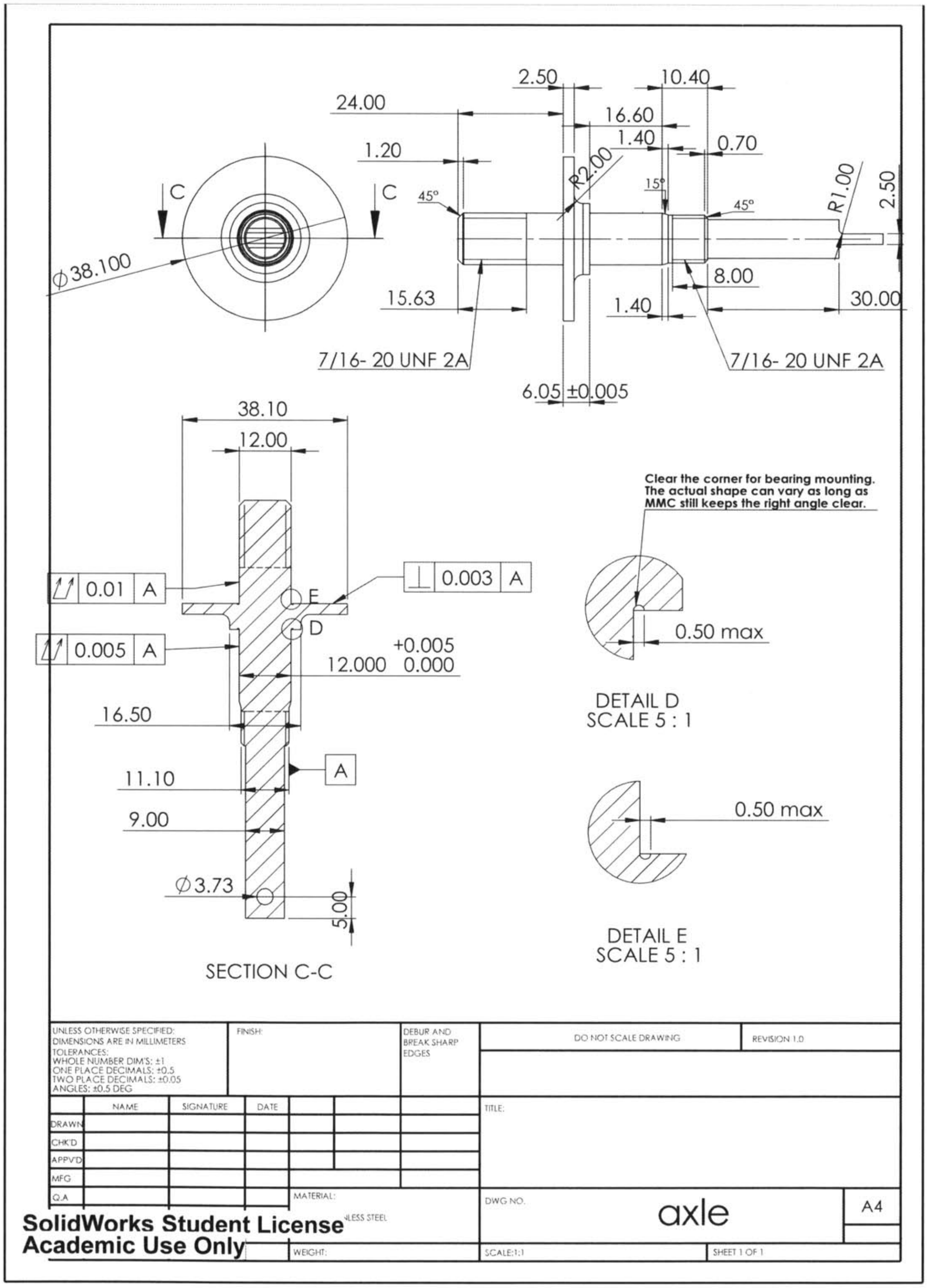
2.50
10.40
24.00
16.60
1.40
1.20
0.70
R2.00
15°
R1.00
2.50
C
C
45°
45°
ϕ38.100
15.63
8.00
1.40
30.00
7/16- 20 UNF 2A
7/16- 20 UNF 2A
6.05 ±0.005
38.10
12.00
0.01 A
0.003 A
E
D
0.005 A
+0.005
12.000 0.000
16.50
A
11.10
9.00
ϕ3.73
5.00
SECTION C-C
Clear the corner for bearing mounting.
The actual shape can vary as long as
MMC still keeps the right angle clear.
0.50 max
DETAIL D
SCALE 5 : 1
0.50 max
DETAIL E
SCALE 5 : 1
UNLESS OTHERWISE SPECIFIED:
DIMENSIONS ARE IN MILLIMETERS
TOLERANCES:
WHOLE NUMBER DIM'S: ±1
ONE PLACE DECIMALS: ±0.5
TWO PLACE DECIMALS: ±0.05
ANGLES: ±0.5 DEG
FINISH:
DEBUR AND
BREAK SHARP
EDGES
DO NOT SCALE DRAWING
REVISION 1.0
NAME
SIGNATURE
DATE
DRAWN
CHK'D
APPV'D
MFG
Q.A
TITLE:
MATERIAL:
LESS STEEL
DWG NO.
axle
A4
WEIGHT:
SCALE:1:1
SHEET 1 OF 1
SolidWorks Student License
Academic Use Only

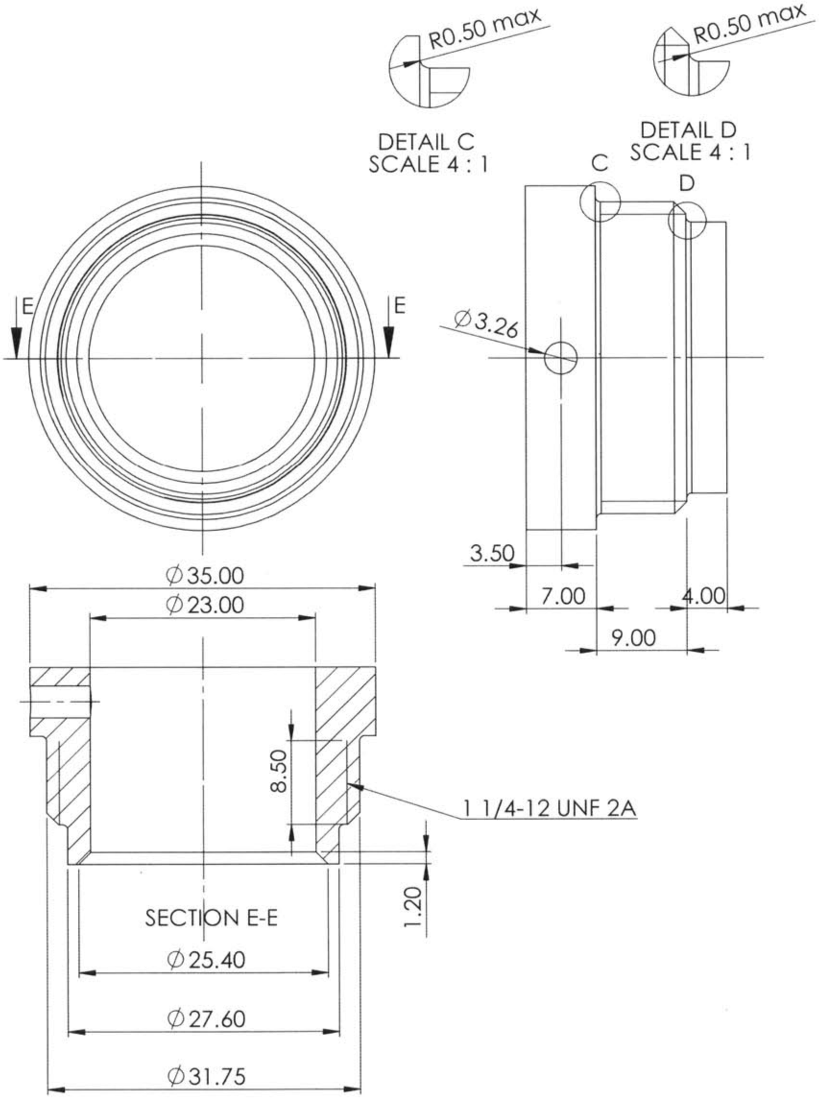
R0.50 max
R0.50 max
DETAIL C
SCALE 4 : 1
DETAIL D
SCALE 4 : 1
C
D
E
E
⌀3.26
3.50
7.00
4.00
9.00
⌀35.00
⌀23.00
8.50
1 1/4-12 UNF 2A
1.20
SECTION E-E
⌀25.40
⌀27.60
⌀31.75

UNLESS OTHERWISE SPECIFIED:
DIMENSIONS ARE IN MILLIMETERS
TOLERANCE:
WHOLE NUMBER DIM'S: ±1
ONE PLACE DECIMALS: ±0.5
TWO PLACE DECIMALS: ±0.05
ANGLES: ±0.5°

FINISH:

DEBUR AND BREAK SHARP EDGES

DO NOT SCALE DRAWING

REVISION 1.0

	NAME	SIGNATURE	DATE
DRAWN			
CHK'D			
APPV'D			
MFG			
Q.A			

TITLE:

MATERIAL:
S STEEL

WEIGHT:

DWG NO. bearingretainer

A4

SCALE:2:1

SHEET 1 OF 1

SolidWorks Student License
Academic Use Only

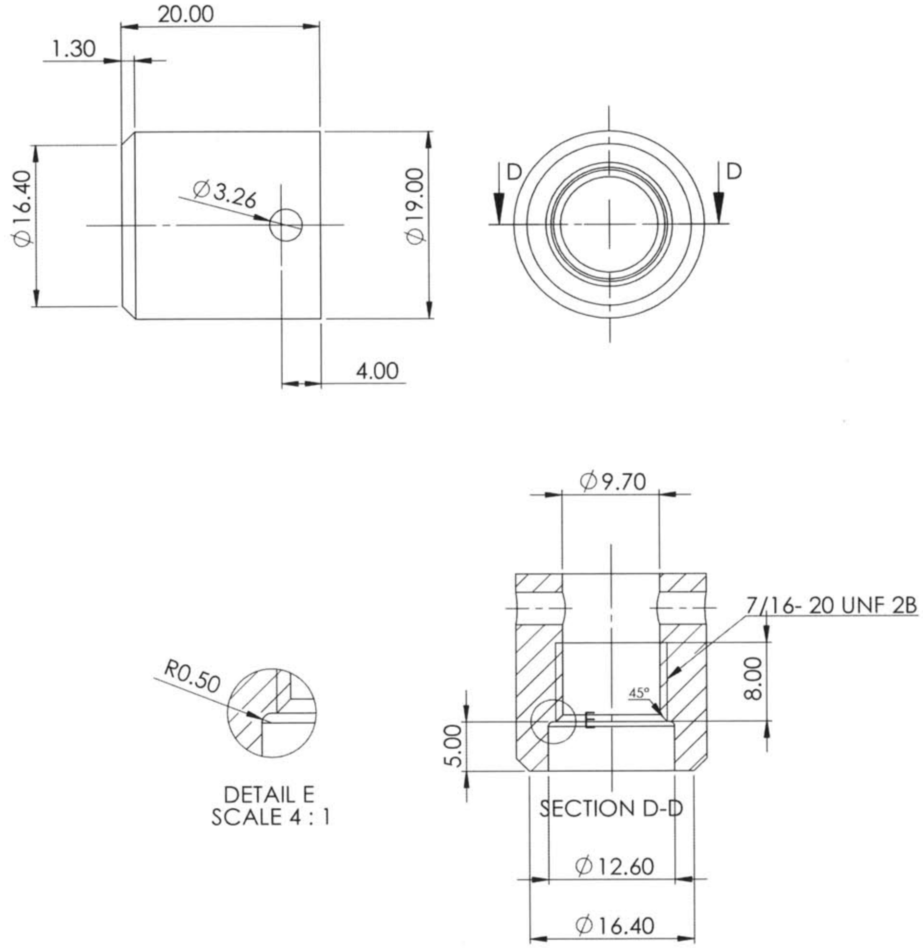

20.00
1.30
Ø16.40
Ø3.26
Ø19.00
4.00
D
D
Ø9.70
7/16- 20 UNF 2B
8.00
45°
E
5.00
R0.50
DETAIL E
SCALE 4 : 1
SECTION D-D
Ø12.60
Ø16.40

UNLESS OTHERWISE SPECIFIED:
DIMENSIONS ARE IN MILLIMETERS
TOLERANCE:
WHOLE NUMBER DIM'S: ±1
ONE PLACE DECIMALS: ±0.5
TWO PLACE DECIMALS: ±0.05
ANGLES: ±0.5 DEG

FINISH:

DEBUR AND BREAK SHARP EDGES

DO NOT SCALE DRAWING

REVISION 1.0

	NAME	SIGNATURE	DATE
DRAWN			
CHK'D			
APPV'D			
MFG			
Q.A			

TITLE:

MATERIAL:
S STEEL

WEIGHT:

DWG NO.
bearinginnerretainer

A4

SCALE:2:1

SHEET 1 OF 1

SolidWorks Student License
Academic Use Only

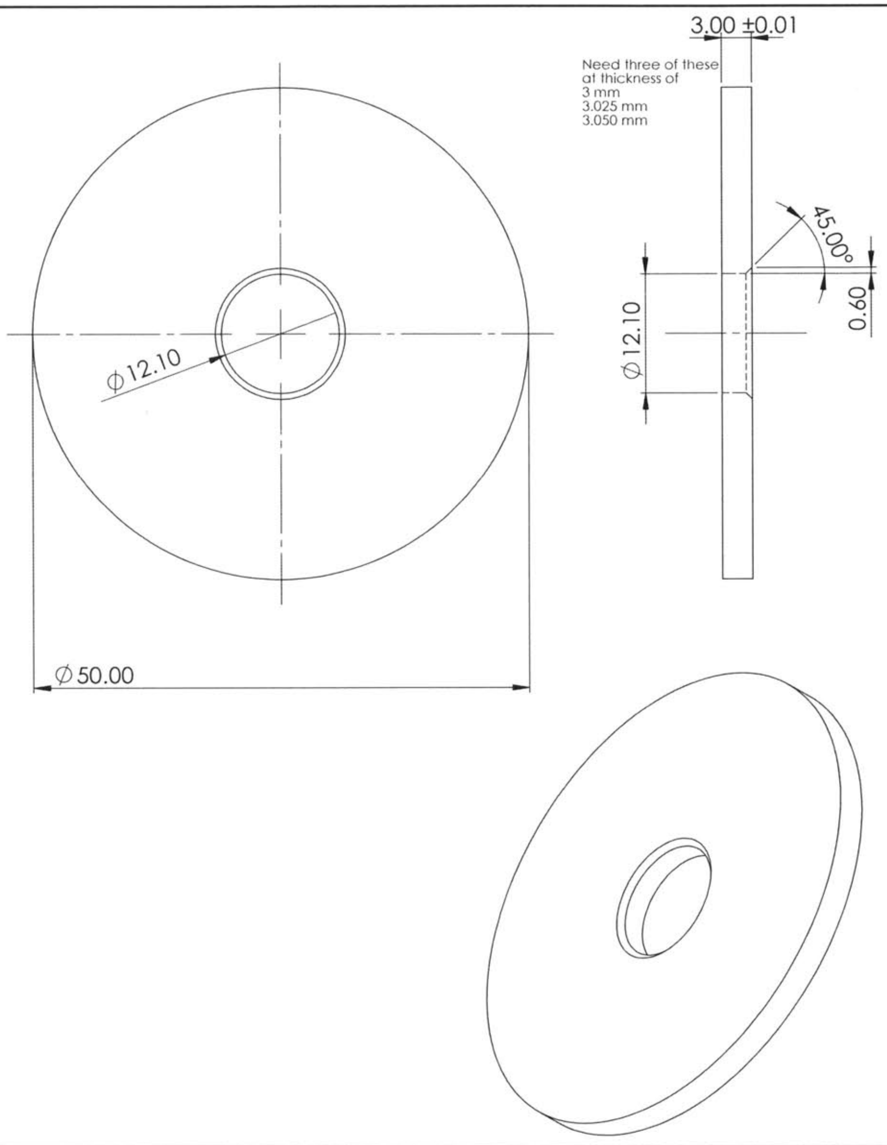

Need three of these
at thickness of
3 mm
3.025 mm
3.050 mm

UNLESS OTHERWISE SPECIFIED:
DIMENSIONS ARE IN MILLIMETERS
TOLERANCE:
WHOLE NUMBER DIM'S: ±1
ONE PLACE DECIMALS: ±0.5
TWO PLACE DECIMALS: ±0.05
ANGLES: ±0.5 DEG

FINISH:

DEBUR AND
BREAK SHARP
EDGES

DO NOT SCALE DRAWING

REVISION

	NAME	SIGNATURE	DATE
DRAWN			
CHK'D			
APPV'D			
MFG			
Q.A			

TITLE:

MATERIAL:
S STEEL

WEIGHT:

DWG NO. rotorstiffener1

A4

SCALE:2:1

SHEET 1 OF 1

SolidWorks Student License
Academic Use Only

Bibliography

[1] *Metals Handbook*, page 792. American Society for Metals, 1966.

[2] Jr. A. E. Fitzgerald, Charles Kingsley and Stephen D. Umans. *Electric Machinery*, chapter 1, pages 1–19. Mc Graw Hill, 2003.

[3] James H. Goldie and James Kirtley. Parallel air gap serial flux a.c. electric machine. Patent No. 5,396,140, March 1995. United States.

[4] James H. Goldie and James Kirtley. Parallel air gap serial flux a.c. electric machine. Patent No. 5,495,131, February 1996. United States.

[5] W. H. Taylor. Obtaining motive power. Patent No. 8255, May 1840. England.

[6] Herbert H. Woodson and James R. Melcher. *Electromechanical Dynamics*, volume 1, chapter 2–3. John Wiley & Sons, 1968.

[7] Herbert H. Woodson and James R. Melcher. *Electromechanical Dynamics*, volume 2, pages 347–357. John Wiley & Sons, 1968.